Article

H-bonded organic frameworks as ultrasound-programmable delivery platform

https://doi.org/10.1038/s41586-024-08401-0

Received: 8 December 2023

Accepted: 14 November 2024

Published online: 5 February 2025

Check for updates

Wenliang Wang[1,7], Yanshu Shi[2,7], Wenrui Chai[3,7], Kai Wing Kevin Tang[1,7], Ilya Pyatnitskiy[1], Yi Xie[2], Xiangping Liu[1], Weilong He[1], Jinmo Jeong[1], Ju-Chun Hsieh[1], Anakaren Romero Lozano[1], Brinkley Artman[1], Xi Shi[4], Nicole Hoefer[5], Binita Shrestha[1], Noah B. Stern[1], Wei Zhou[6], David W. McComb[5], Tyrone Porter[1], Graeme Henkelman[3], Banglin Chen[2]✉ & Huiliang Wang[1]✉

The precise control of mechanochemical activation within deep tissues using non-invasive ultrasound holds profound implications for advancing our understanding of fundamental biomedical sciences and revolutionizing disease treatments[1–4]. However, a theory-guided mechanoresponsive materials system with well-defined ultrasound activation has yet to be explored[5,6]. Here we present the concept of using porous hydrogen-bonded organic frameworks (HOFs) as toolkits for focused ultrasound (FUS) programmably triggered drug activation to control specific cellular events in the deep brain, through on-demand scission of the supramolecular interactions. A theoretical model is developed to potentially visualize the mechanochemical scission and ultrasound mechanics, providing valuable guidelines for the rational design of mechanoresponsive materials to achieve programmable control. To demonstrate the practicality of this approach, we encapsulate the designer drug clozapine N-oxide (CNO) into the optimal HOF nanocrystals for FUS-gated release to activate engineered G-protein-coupled receptors in the ventral tegmental area (VTA) of mice and rats and hence achieve targeted neural circuit modulation even at depth 9 mm with a latency of seconds. This work demonstrates the capability of ultrasound to precisely control molecular interactions and develops ultrasound-programmable HOFs to non-invasively and spatiotemporally control cellular events, thereby facilitating the establishment of precise molecular therapeutic possibilities.

An optimal delivery system should non-invasively and precisely target the specific tissues or cells involved in the disease, achieving a concentration and duration that yield the intended physiological response without excess or inadequate effect[5,7]. This precision is essential for a wide range of disease treatments, from temporal activation for neural activity modulation[3,8], gradual release for treating chronic pain[9] or the sequential control of drugs at various disease progression stages[10]. Cutting-edge technologies such as optogenetics have empowered scientists to execute sophisticated molecular manipulations of opsins at specific cells or projections, substantially advancing our understanding of brain processes and offering the potential for on-demand treatment of neural diseases[11]. However, their application in deep tissue is constrained owing to the inefficient delivery of photons within organisms. Non-invasive molecular manipulation holds great promise for clinical therapeutic applications.

FUS presents a unique opportunity for non-invasive control in deep tissue with millimetric spatial precision and exemplary safety[1,4,12–14]. Ultrasound-triggered phase-shift microbubbles, nanoemulsions and sonosensitized liposomes have been developed as promising candidates in mechanotherapy and local anaesthesia[3,15–17]. Furthermore, scientists have recently demonstrated the potential of ultrasound to selectively cleave labile covalent or non-covalent bonds from mechanosensitive rotaxane actuator or polymer frameworks, creating new opportunities for precise drug manipulation at the molecular level[1,2,18]. However, the presence of strong covalent and non-covalent bonds within polymer frameworks often necessitates high ultrasound power densities, resulting in extended response times on the order of hours[18–22]. More importantly, the topologically complex nature of these systems poses challenges in establishing a theoretical system to visualize the intrinsic relationships between scission efficiency, framework molecular structure and ultrasound power[23,24]. Despite notable progress in ultrasound-triggered systems, a comprehensive model has yet to be developed to explain the manipulation at the molecular level induced by ultrasound (Supplementary Table 1). The development of ultrasound-programmable systems with tunable structural stability and ultrasound sensitivity are still challenging.

Porous frameworks, including metal–organic frameworks and covalent organic frameworks, have gained great attention as drug-delivery platforms owing to their excellent drug-loading capacity and well-defined structures[25,26]. Among them, HOFs have recently emerged as a

[1]Biomedical Engineering, Cockrell School of Engineering, The University of Texas at Austin, Austin, TX, USA. [2]Department of Chemistry, The University of Texas at San Antonio, San Antonio, TX, USA. [3]Freshman Research Initiative, College of Natural Sciences, The University of Texas at Austin, Austin, TX, USA. [4]Department of Molecular Biosciences, The University of Texas at Austin, Austin, TX, USA. [5]Center for Electron Microscopy and Analysis, The Ohio State University, Columbus, OH, USA. [6]Center for Neutron Research, National Institute of Standards and Technology, Gaithersburg, MD, USA. [7]These authors contributed equally: Wenliang Wang, Yanshu Shi, Wenrui Chai, Kai Wing Kevin Tang. ✉e-mail: banglin.chen@utsa.edu; evanwang@utexas.edu

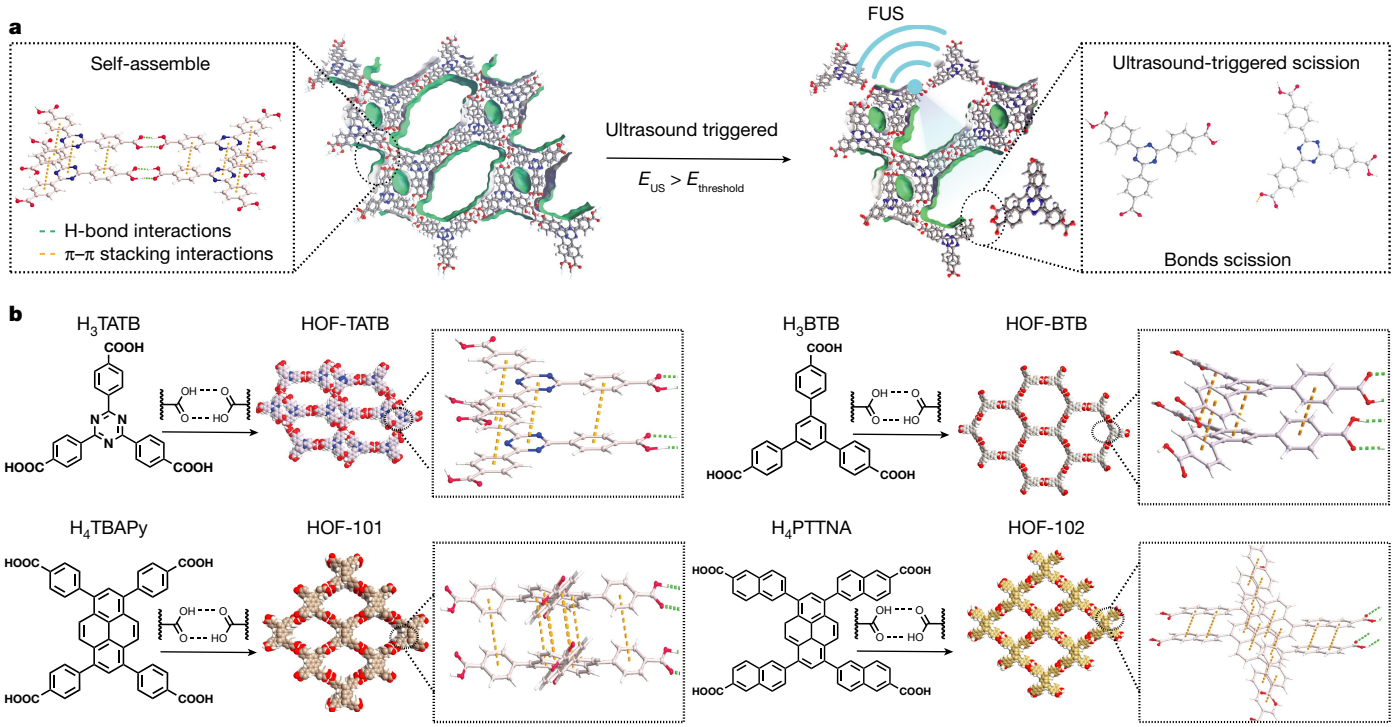

Fig. 1 | Ultrasound mechanically responsive HOFs preparation. a, Schematic illustration of the ultrasound mechanical stress triggered dissociation of HOFs, in which the HOFs were stable in solution but disassociated when triggered by the ultrasound power (E_{US}) exceeding the HOFs scission threshold ($E_{US} > E_{threshold}$). **b**, Four representative organic monomers and the self-assembled porous HOF structures: HOF-TATB, HOF-BTB, HOF-101 and HOF-102. The OMBUs of HOFs self-assemble through hydrogen bonding and π–π stacking interactions, resulting in the formation of 3D porous frameworks.

particularly promising class of porous materials with both high structural homogeneity and programmability, self-assembled from organic molecular building units (OMBUs) through hydrogen bonding and π–π stacking interactions[27]. Unlike strong metal–ligand coordination and covalent bonding interactions in metal–organic frameworks and covalent organic frameworks, the relatively weak non-covalent interactions makes HOFs excellent candidates for mechanochemical activation under FUS stimulation. Also, the abundant diversity of building units make HOFs easily tunable in terms of their compositions and functionalities for carter custom-design applications[28]. If the HOFs can be precisely tailored and selectively activated through non-invasive ultrasound, this system could facilitate remote medication manipulation, offering precise disease treatment in deep tissue, particularly for sophisticated neuronal modulation in the deep brain.

Characterization of mechanoresponsive HOFs

We investigated the potential of HOF nanocrystals to function as mechanoresponsive platforms, enabling ultrasound-programmable and selective activation by adjusting the framework building units (Fig. 1a). Specifically, we targeted four different OMBUs with varying density of hydrogen bonding and aromatic rings in respective building units for the synthesis of four porous HOF nanocrystals, HOF-TATB, HOF-BTB, HOF-101 and HOF-102 (Fig. 1b). The nuclear magnetic resonance spectra of corresponding OMBUs are shown in Supplementary Figs. 1–4. We used a precipitation method to produce HOF nanocrystals. Both dynamic light scattering (DLS) and transmission electron microscopy (TEM) analyses confirmed the successful fabrication of HOF nanocrystals (Extended Data Fig. 1a–d and Supplementary Table 2). The results showed that the size of these HOF nanocrystals ranged from 250 to 600 nm, with a polydispersity index of approximately 0.2 to 0.3, as presented in Supplementary Table 2.

Owing to the planar nature, the OMBUs spontaneously assembled into 2D layers by means of classic carboxylic acid hydrogen-bonded $R_2^2(8)$ dimers, in which the tetracarboxylic OMBUs form a square lattice topology layer in HOF-101 and HOF-102. More specifically, the strong π–π stacking of pyrene moieties in HOF-101 and HOF-102 drives the 2D square layers to further stack with adjacent layers into 3D crystals with rhombus 1D channel[29,30] (Fig. 1b and Supplementary Table 3). The layers of self-assembled tricarboxylic acids in HOF-BTB are first stacked to align the aromatic motifs and further interwoven to maximize the overall molecular packing[31]. The crystal structure of HOF-BTB, HOF-101 and HOF-102 were previously reported and the phase purity was confirmed by the powder X-ray diffraction[29–31] (Extended Data Fig. 1e–h). We note that the crystal structure of downsized HOF-TATB nanocrystals has yet to be reported, which herein was determined by microcrystal electron diffraction (microED; Extended Data Fig. 2, Supplementary Fig. 5 and Supplementary Table 4). In HOF-TATB, H_3TATB OMBUs self-assemble into a doubly interpenetrated 3D hydrogen-bonded (3,4)-nets through two types of intermolecular hydrogen-bonding motif and inclined π–π stacking (Extended Data Fig. 2a and Supplementary Fig. 5). Other than the typical carboxylic acid dimer (O···H–O 2.675–2.686 Å) formed by one of the three carboxylic acids, the other two carboxylic acid groups participate in the formation of a unique hydrogen-bonded $D_4^4(15)$ tetramer motifs (O···H–O 2.575–2.762 Å) with a dangling weak hydrogen bond with guest methanol and the adjacent tetramer in the neighbouring interpenetrated net (O···H–O 3.051–3.767 Å) (Supplementary Fig. 5 and Extended Data Fig. 2b,c). The tetramer motifs from two interpenetrated nets are associated by the inversion centre rendering an inclined stacked geometry of H_3TATB molecules with a distance of 3.32 Å. On removal of the guest solvents, HOF-TATB exhibits a 1D pore channel along the crystallographic *b* axis of size 12.2 × 23.9 Å and a 50.3% solvent-accessible void of the crystal volume, indicating excellent potential for drug-loading properties (Extended Data

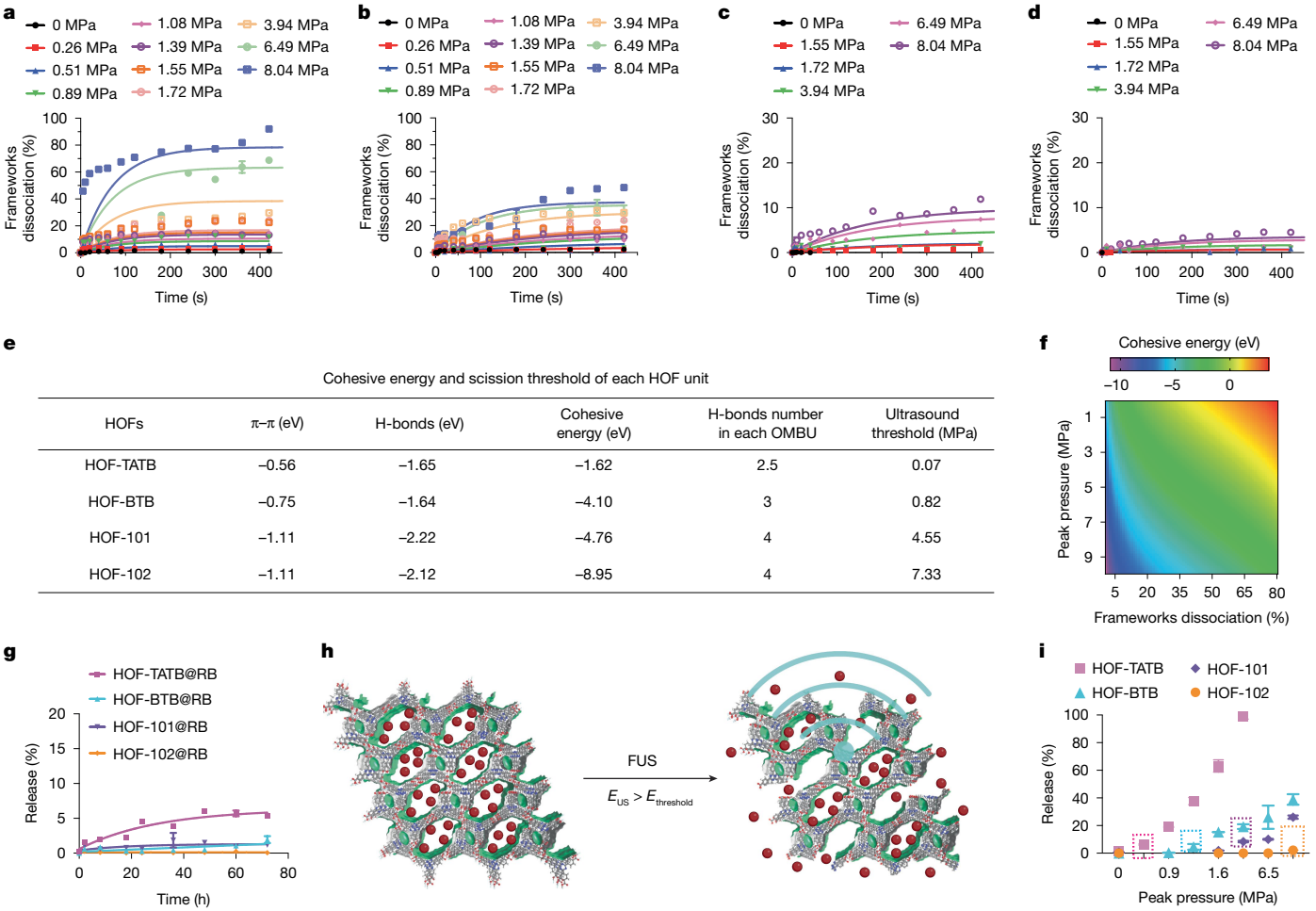

Fig. 2 | Ultrasound mechanically controlled dissociation of HOFs in an aqueous solution. a–d, Ultrasound mechanically triggers the time-resolved dissociation curve of different HOFs (mean ± s.e.m., $n = 3$ independent experiments for each sample) at various peak pressures, including HOF-TATB (**a**), HOF-BTB (**b**), HOF-101 (**c**) and HOF-102 (**d**). **e**, Cohesive energy of different HOFs, including their hydrogen-bonding interactions and π–π stacking interactions in each unit. HOFs were constructed from organic building units through intermolecular non-covalent hydrogen-bonding interactions and π–π stacking interactions, for which the bonding energy of one unit was denoted as the cohesive energy of HOFs. Moreover, the HOFs showed varying ultrasound thresholds for dissociation, which were associated with the characteristics of the organic building units. **f**, The prediction heat map of ultrasound-controlled dissociation of HOFs. By referring to the provided heat map, we can determine the optimal cohesive energy needed to attain a dissociation percentage at a specific ultrasound power. This will guide the structural design of HOFs at the molecular level to achieve the cohesive energy required for subsequent programmable control of HOFs dissociation at certain ultrasound peak pressures. **g**, The free dye release from HOF nanocrystals without ultrasound stimulation (mean ± s.e.m., $n \geq 3$ independent experiments for each sample). **h**, Schematic of ultrasound-triggered drug release from HOF nanocrystals, with drug release occurring when $E_{US} > E_{threshold}$. **i**, Ultrasound-triggered dye release from HOF nanocrystals after 90 s of stimulus (mean ± s.e.m., $n \geq 3$ independent experiments for each sample). The HOF nanocrystals exhibited distinct ultrasound thresholds for drug activation, with the order of sensitivity being HOF-TATB@RB (0.51 MPa) < HOF-BTB@RB (1.55 MPa) < HOF-101@RB (3.94 MPa) < HOF-102@RB (8.04 MPa).

Fig. 2d–h). The bulk purity and prolonged hydrolytic stability (up to 1 week) of as-synthesized HOF-TATB nanocrystals were confirmed by powder X-ray diffraction (Supplementary Fig. 6). The 77-K N_2 or 195-K CO_2 adsorption isotherms of four HOFs demonstrated their porous structures (Extended Data Fig. 3a–d and Supplementary Table 5).

Next we verified the ultrasound-triggered scission of HOF nanocrystals in an aqueous medium by monitoring the framework dissociation percentage over time (Fig. 2a–d and Supplementary Figs. 7–10). Following ultrasound stimulation, the OMBUs cleaved from the HOFs were dissolved and found in the supernatant after centrifugation. Their concentration was then measured using UV-Vis spectroscopy to calculate the framework dissociation percentage (Supplementary Figs. 7–10). The results indicated that different HOFs exposed to ultrasound with varying peak pressures will reach characteristic dissociation equilibrium, as illustrated in Fig. 2a–d and Supplementary Figs. 7–10. For instance, irradiation of the HOF nanocrystals with ultrasound (1.5 MHz) at a power of 8.04 MPa led to approximately 91.8%, 45.3%, 11.6% and 4.7% dissociation after equilibrium in HOF-TATB, HOF-BTB, HOF-101 and HOF-102, respectively. This suggests that the ultrasound-triggered HOF dissociation may be a thermodynamic process (as discussed in the Supplementary information). However, no obvious dissociation was observed even when these HOFs were heated at 100 °C for 5 min, demonstrating their high thermal stability (Extended Data Fig. 4a–d). These results determined that the ultrasound stress, rather than the thermal effect, constitutes the main driving force to shear the intramolecular non-covalent bonds and dissociate the frameworks. In fact, HOFs demonstrate an excellent capability for ultrasound power programmable behaviour through mechanochemical activation. Activation of HOFs occurs exclusively when the ultrasound power reaches a specific peak pressure, with the ultrasound power activation thresholds being contingent on the type of OMBU used (Fig. 2a–d). Also, the dissociation percentage

increases in response to higher ultrasound peak pressure for all four different HOFs, with difference in increasing rate depending on the specific type of HOF, as shown in Fig. 2a–d. We call this approach 'UltraHOF', an abbreviation of ultrasound-programmable activation of HOFs.

Theoretical modelling of mechanochemical scission

Next we initiated efforts to explain this ultrasound-triggered and programmable dissociation process. The structure–property relationships of the HOFs were investigated using density functional theory (DFT) calculations, by calculating the cohesive energy ($E_{cohesive}$, the energy needed to dissociate the HOF crystals into isolated building units) of, from the lowest to the highest, HOF-TATB, HOF-BTB, HOF-101 and HOF-102 in solution, indicating increasing relative stability of the HOFs (Fig. 2e). This observation is consistent with the experimental findings in which the dissociation equilibrium constant (k, the ratio of dissociated HOF building units percentage to undissociated HOF percentage at certain ultrasound pressure) decreases sequentially in these four HOFs (Supplementary Table 6). Gibbs free energy provides a means of defining equilibrium or the tendency of a reaction. In the context of the ultrasound-triggered HOF dissociation process, the acoustic field can be considered to alter the reaction free energy change. Consequently, the change in ln(k) should exhibit a correlation with ultrasound power. The experimental data showed an approximate linear correlation between the ultrasound peak pressure and ln(k), as illustrated in Extended Data Fig. 5a,b, supporting the notion that the ultrasound-triggered dissociation of HOF is indeed a thermodynamic process. Our reaction model indicated an approximate linear relationship between ln(k) and $E_{cohesive}$ of the HOFs (Extended Data Fig. 5c) and thus we can extrapolate the required minimum $E_{cohesive}$ of HOFs at any desired ln(k). Furthermore, we found a linear relationship between the required minimum $E_{cohesive}$ and the ultrasound peak pressure (E_{US}) of the HOFs at any ln(k) (Extended Data Fig. 5d and Supplementary Tables 6 and 7). From these linear relationships between ln(k) and $E_{cohesive}$ and between E_{US} and $E_{cohesive}$, we developed a preliminary three-variable model to represent how these variables are correlated. The heat map in Fig. 2f potentially predicts the $E_{cohesive}$ of HOFs needed for achieving a given dissociation percentage at a specific ultrasound power, thus providing a guideline for designing HOFs for on-demand drug activation by ultrasound. From the prediction model, we also estimated the theoretical ultrasound power thresholds (the minimum ultrasound peak pressure to achieve 3% dissociation of HOFs) for HOF-TATB, HOF-BTB, HOF-101 and HOF-102 as 0.07, 0.82, 4.55 and 7.33 MPa respectively (Fig. 2e and Supplementary Fig. 11). It is crucial to acknowledge that our theory serves as a qualitative framework rather than a quantitative model. Other factors, such as crystal defects in the frameworks and acoustic cavitation efficiency, may also play important roles in influencing ultrasound-triggered HOF dissociation. Our simplified analysis provides a valuable first-order approximation for explaining this ultrasound-programmable mechanochemical process in HOFs. Because the sensitivity of HOFs to ultrasound is governed by the overall strength of weak interactions encoded in the HOF structure, primarily contributed by hydrogen bonds and π–π interactions among OMBUs, the relationship between the OMBU structures and ultrasound sensitivity is important for explaining the acoustic scission principles of HOFs at the molecular level. The DFT results (Fig. 2e) show that the hydrogen-bonding energy (E_{HB}, the energy per hydrogen-bonded dimer) is approximately −1.1 eV and remains relatively stable across the molecular structures of the OMBU in the four HOFs. However, the number of hydrogen bonds in each OMBU varies with the carboxyl groups. Specifically, the average number of hydrogen bonds per ligand contributing to the formation of HOF-TATB, HOF-BTB, HOF-101 and HOF-102 is approximately 2.5, 3, 4 and 4, respectively (Fig. 2e). This difference contributes to the higher energy in HOF-BTB, HOF-101 and HOF-102 compared with HOF-TATB. Notably, the increased number of hydrogen bonds in each OMBU substantially enhances the ultrasound-triggered stability of HOF nanocrystals. For π–π interactions, the energy ($E_{π\text{-}π}$) varies with the structure of the OMBU. Higher $E_{π\text{-}π}$ was found in HOF-101 and HOF-102 owing to the increased number of aromatic fused rings in the OMBU (Fig. 2e). Because mechanochemical bond scission is more likely to occur in weak bonds to trigger the dissociation of frameworks, it is reasonable to suggest that the OMBUs with fewer hydrogen bonds and aromatic fused rings in the backbone should be used for HOFs with a higher ultrasound sensitivity.

Ultrasound-programmable drug activation using HOFs

These HOF nanocrystals exhibited outstanding drug-loading capacity. As shown in Supplementary Table 8, the loading capacity increased in HOF-TATB (15.1 ± 1.4%), HOF-BTB (15.8 ± 2.7%), HOF-101 (27.0 ± 1.5%) and HOF-102 (29.8 ± 1.3%). This characteristic reduces the drug carriers needed in delivering specific drug concentrations, thereby minimizing the side effects. We next used dye-release experiments to examine the free drug release of the HOF nanocrystals without ultrasound application (Fig. 2g). Specifically, only 5.5 ± 0.1% of the dye was prematurely released from HOF-TATB nanocrystals without ultrasound even after 3 days of incubation, and the premature release percentage of dye could be reduced further to 1.9 ± 0.9%, 1.2 ± 0.2% and 0.1 ± 0.1% in HOF-BTB, HOF-101 and HOF-102 owing to their increased $E_{cohesive}$. Also, ultrasound-triggered release experiments demonstrated that the percentage of drug released increased with the ultrasound peak pressure used and the type of HOF with lower $E_{cohesive}$ (Fig. 2h,i and Extended Data Fig. 6a–d), consistent with the theoretical ultrasound power thresholds conducted from our prediction model (Fig. 2f). Of note, among various HOF nanocrystals, HOF-TATB nanocrystals exhibited the highest sensitivity to ultrasound, providing optimal temporal resolution for drug activation gating with minimum ultrasound pressure, whereas HOF-102 nanocrystals exhibited the highest stability and drug-loading capacity (Extended Data Fig. 6a–d and Supplementary Table 8). To demonstrate UltraHOF for deep brain stimulation with high temporal resolution, we decided to use HOF-TATB to minimize the ultrasound pressure.

After drug loading, HOF-TATB nanocrystals did not show any notable alterations in size and morphology (Fig. 3a). Furthermore, their negative surface potential ensured excellent biostability, even in the presence of 10% foetal bovine serum (Supplementary Fig. 12). However, it is worth noting that, as the size decreased, there were morphological changes of HOF nanocrystals after exposure to ultrasound stimulation (Fig. 3a and Supplementary Table 2). We observed that drug release was triggered under ultrasound stimulation within a clinically safe range (1.5 MHz, 1.5 MPa), whereas no notable release occurred without ultrasound (Fig. 3b and Extended Data Fig. 6e–h). The percentage of released drugs also increases with the ultrasound peak pressure, with an activation threshold of around 0.51 MPa (Fig. 3c and Extended Data Fig. 6e–h). Moreover, dye release could be repeatedly triggered from the HOF-TATB nanocrystals by a repeated stimulus (10-s pulse), resulting in an example of four triggerable events releasing 10.2 ± 1.3%, 5.0 ± 3.0%, 6.5 ± 5.2% and 10.0 ± 4.4%, respectively (Fig. 3d). We also determine that the payload release percentage increases linearly with the dissociation percentage of the framework (Supplementary Fig. 13). The HOFs also demonstrated great potential as a universal drug-delivery system for ultrasound-programmable activation of various drugs. As shown in Extended Data Fig. 7a–c, drugs such as deschloroclozapine (another potent and selective chemogenetic drug), dopamine (an essential neurotransmitter related to addiction and treatment of Parkinson's disease) and procaine (a drug used for pain management) were effectively loaded into the frameworks. The drug-loading contents were

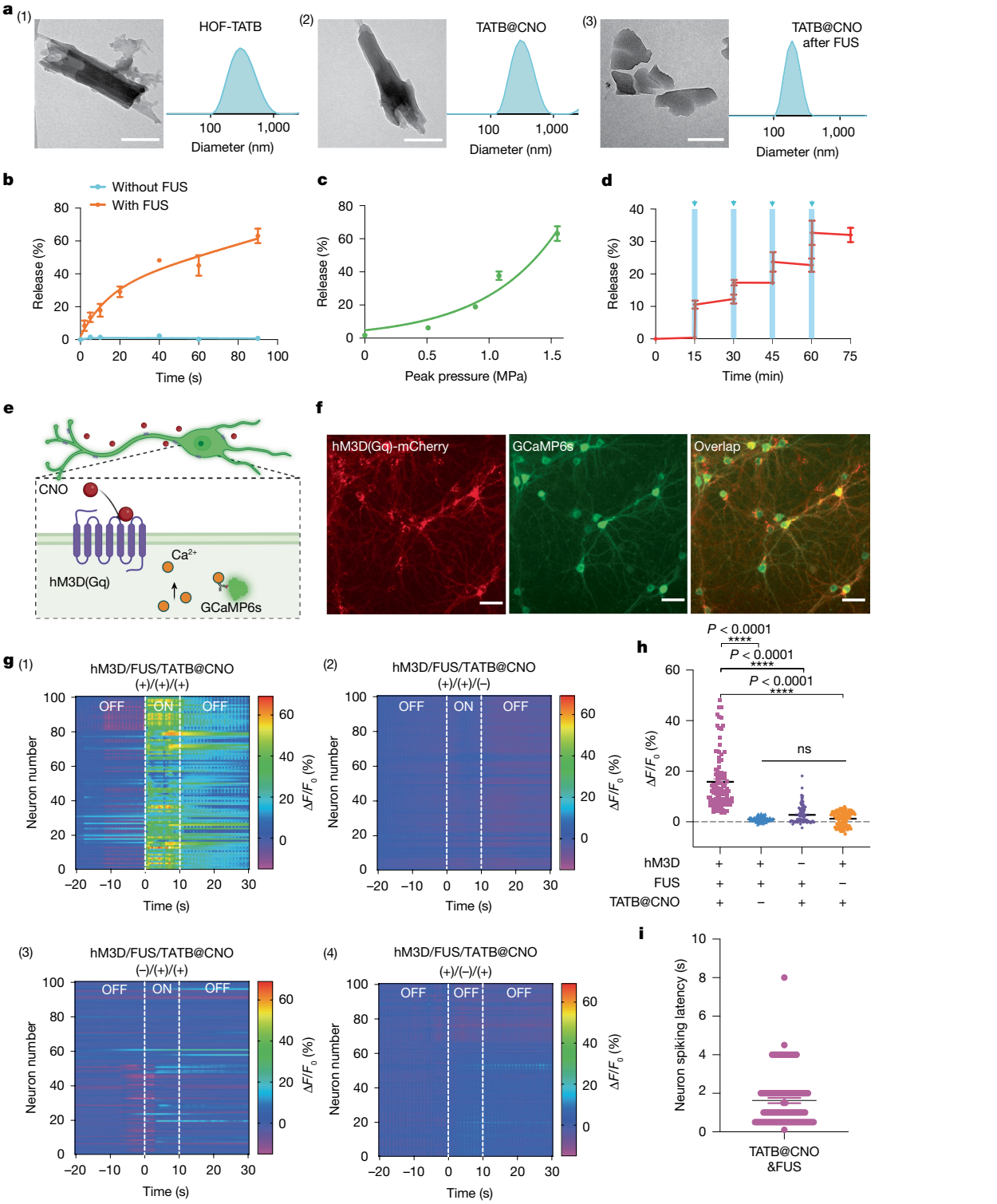

Fig. 3 | Ultrasound-controlled cargo release from HOF-TATB nanocrystals and their in vitro modulation of neural activity. a, TEM images and hydrodynamic size distribution measured by DLS of the HOF-TATB nanocrystals: (1) before loading of CNO, (2) after loading CNO and (3) after irradiating by ultrasound (1.5 MHz, 1.55 MPa, 60 s). Scale bars, 200 nm. $n = 3$ per group. **b**, Ultrasound-triggered dye release (mean ± s.e.m., $n = 3$ independent samples) from HOF-TATB at 1.5 MHz, 1.55 MPa. **c**, Ultrasound-triggered dye release (mean ± s.e.m., $n = 3$ independent samples) from HOF-TATB after 60 s irradiation (1.5 MHz) at different peak pressures. **d**, Repeated ultrasound-triggered drug release. The blue areas indicate ultrasound stimulus (1.5 MHz, 1.55 MPa, pulse 10 s). Mean ± s.e.m., $n \geq 3$ independent tests. **e**, Ultrasound-triggered CNO release from the HOF-TATB nanocrystals for hM3D(Gq) expressing neuron activation. **f**, Fluorescence images of the primary cortical neurons expressing hSyn::hM3D(Gq)-mCherry and hSyn::GCaMP6s-WPRE-SV40. Scale bars, 40 μm. $n = 3$ per group. **g**, Heat maps of normalized GCaMP6s fluorescence intensity from 100 neurons in different experimental conditions ($n = 100$ neurons examined over three independent experiments for each group), including (1) hM3D(+)/FUS(+)/TATB@CNO(+), (2) hM3D(+)/FUS(+)/TATB@CNO(–), (3) hM3D(–)/FUS(+)/TATB@CNO(+) and (4) hM3D(+)/FUS(–)/TATB@CNO(+). OFF = ultrasound off; ON = ultrasound on (1.5 MHz, 1.08 MPa, 10 s pulse). **h**, Statistical analysis of calcium signal changes in 100 primary neurons under the different conditions ($n = 100$ neurons examined over three independent experiments for each group). Mean ± s.e.m. Two-way ANOVA and Tukey's tests ($P \geq 0.05$ (ns), ****$P < 0.0001$). **i**, Normalized in vitro neuron spiking latency under sono-chemogenetics stimulation. $n = 100$ neurons examined over three independent experiments for each group. Mean ± s.e.m.

measured at 9.7 ± 0.9 wt%, 7.8 ± 0.5 wt% and 4.8 ± 1.2 wt%, respectively, and were successfully gated through ultrasound for on-demand release. Furthermore, we determined the biosafety of the HOF-TATB nanocrystals through the haemolysis and cell viability tests (Extended Data Fig. 8a–c). The results showed no apparent toxicity or haemolysis, even at high concentrations. This suggested that our HOF-TATB nanocrystals are generally biocompatible and biosafe as drug-delivery platforms.

Sono-chemogenetics for deep brain stimulation

Chemogenetics used engineered G-protein-coupled receptors to activate neurons on specific drugs agonists binding, exhibiting unique advantages for long-period neuromodulation and minimum immunogenicity compared with optogenetics[32,33]. However, conventional chemogenetics is often limited by off-target effects and low temporal resolution dependent on pharmacokinetics[34,35]. Recent advancements in remote and minimally invasive control over drug activation offer considerable potential for clinical therapeutic applications in chemogenetics[4,36], whereas the limited temporal control of drug activation and constrained working range in brain tissue still pose substantial challenges for achieving precise temporal control of neural activity (Supplementary Table 9). To address these challenges, we developed our UltraHOF technology for precise activation of the designer drug CNO, aiming to achieve high temporal resolution in deep brain regions.

We applied our HOF-TATB nanocrystals for the loading of CNO (TATB@CNO) for ultrasound-triggered release of CNO to activate designer receptors exclusively activated by designer drugs in cultured neurons (Fig. 3e and Extended Data Fig. 7d). First, the neurons were transduced with endogenous designer receptors hM3D(Gq) with red fluorescent reporter mCherry (AAV-9-hSyn-hM3D(Gq)-mCherry) and green fluorescence calcium indicator (AAV-9-hSyn-GCaMP6s-WPRE-SV40), as shown in Fig. 3f. We initially validated the activation of hM3D(Gq) expressing neurons with the free designer drug CNO using fluorescence imaging of GCaMP6s calcium indicators (Supplementary Fig. 14). Then, by subjecting CNO-encapsulating nanocrystals (TATB@CNO) to ultrasound irradiation, more than 90% of hM3D(Gq)$^+$ neurons fired with a latency of 1.6 s and continuously activated for about 60 s. However, only sporadic neuronal activation was observed in the absence of ultrasound stimulus, hM3D(Gq) expression or TATB@CNO (Fig. 3g–i and Supplementary Fig. 15). The burst release of CNO from HOF-TATB nanocrystals under ultrasound stimulus enables the rapid triggering of hM3D(Gq), inducing long-term (>60 s) neuron membrane depolarization. Our UltraHOF-enabled sono-chemogenetics provides a new method for achieving fast and continuous neuronal activation with minimal invasiveness.

Precisely timed activation of genetically targeted neurons is important for researchers to understand the links between brain activity and behaviour[11]. We subsequently assessed real-time UltraHOF-enabled sono-chemogenetic neural excitation through fibre photometry in the VTA of mice, a region known for its role in regulating reward learning and depression[37]. Ultrasound energy propagates through tissue as a travelling pressure wave, with penetration depth increasing with lower frequency but at the cost of decreased resolution[38]. In our experiments, a 1.5-MHz transducer achieved a maximum penetration depth of 20 mm, with 37% delivery efficiency at a tissue depth of 10 mm (Extended Data Fig. 9a). The ultrasound energy heat map in the mouse brain showed that a primary power of 1.4 MPa produced an acoustic pressure of around 0.9 MPa at the VTA of mice (Extended Data Fig. 9b), which is sufficient to activate CNO release (Fig. 3c and Extended Data Fig. 6e–h). We performed unilateral transduction of neurons in the VTA using the AAV-9-hSyn-hM3D(Gq)-mCherry and AAV-9-hSyn-GCaMP6s-WPRE-SV40 virus, followed by the injection of TATB@CNO in the same region 4 weeks later (Fig. 4a,b). We used fibre photometry to record Ca^{2+}-influx-induced GCaMP6s signal increase in mice to assess neuronal excitation in response to ultrasound-gated release of CNO after 2 days of injection. The GCaMP6s signal increased markedly on ultrasound irradiation of the VTA region for neurons with hM3D(Gq) expression but remained unchanged without hM3D(Gq) expression, TATB@CNO nanocrystals or ultrasound stimulus (Fig. 4c,d). Our sono-chemogenetics approach demonstrated high temporal resolution, with a 3.5-s latency for neural activations on ultrasound stimulus (Fig. 4e). We observed more than 120 s of continuous excitation of neural activity with each 10-s sono-chemogenetic stimulation and several increases in GCaMP6s fluorescent signal were observed on repeated exposure to ultrasound even after 5 days following injection owing to the long-term biostability of TATB@CNO in the brain (Supplementary Figs. 16 and 17). Immunofluorescence analysis of the expression of c-fos, an immediate early gene and a marker for neural excitation[39], further showed that neurons excitation in the VTA was only triggered by the FUS stimulus in mice with both expression of hM3D(Gq) and injected TATB@CNO nanocrystals (Fig. 4f,g).

On the basis of the notable neural excitation observed in the VTA, we subsequently assessed the ability of UltraHOF-enabled sono-chemogenetics in modulating the reward-learning behaviour of mice (Fig. 4h). After injecting TATB@CNO into the VTA region with hM3D(Gq) expression on day 0, mice were allowed to freely explore the apparatus without any stimulus on day 2 (pre-tests). On day 3, mice received sono-chemogenetic stimulus (1.5 MHz, pulse 20 s, 1.40 MPa) in the designated conditioned chambers with two sessions. On day 4, mice again freely explored the apparatus without any stimulus (post-test). Trail tracing showed that mice expressing hM3D(Gq) preferentially explored the conditioned side of the apparatus after receiving sono-chemogenetics (Fig. 4i), resulting in an approximately twofold increase in time spent in the conditioned chamber (Fig. 4j). Notably, in the absence of hM3D(Gq) expression, TATB@CNO or ultrasound stimulus, the preference did not vary substantially in the experimental trial (Fig. 4j,k).

On the basis of previous evidence of the antidepressant effects of neural activity in the VTA[37], we aimed to investigate whether UltraHOF-enabled sono-chemogenetics could affect mouse behaviour in the forced swim test (FST). To achieve this, VTA neurons were transduced with hM3D(Gq) and mice were allowed to recover from TATB@CNO VTA injection surgery (day 0) for 2 days before undergoing a 5-min pre-FST test (day 2). On day 3, mice received ultrasound stimulus (1.5 MHz, pulse 20 s, 1.40 MPa) before the 5-min FST assay (Fig. 4l). We tracked the swimming patterns of the mice during the FST period using motion cameras. The results showed that hM3D(Gq)$^+$ mice exhibited increased activity, that is, increased swimming distance during the FST period (Fig. 4m). Furthermore, the dynamic motion analysis showed that hM3D(Gq)$^+$ mice exhibited higher mobility throughout the FST period, with a slight increase in immobility preference only after swimming for 2 min. On the other hand, in the absence of hM3D(Gq) expression, TATB@CNO or ultrasound stimulus, the immobility time greatly increased in mice (Fig. 4n,o). These findings suggest that UltraHOF-enabled sono-chemogenetics can effectively modulate mouse behaviour in the FST. After 14 days of stimulation, we also evaluated the in vivo biocompatibility of our sono-chemogenetics approach by immunostaining brain sections. These results demonstrate that this approach did not cause any notable cell toxicity through haematoxylin and eosin staining (Extended Data Fig. 8d). Also, we did not observe any activation of microglia or astrocytes, nor did we detect any neuron apoptosis (Extended Data Fig. 8e–g and Supplementary Figs. 18–20). Furthermore, we did not observe any evident blood–brain barrier opening and uncontrollable thermal effects at the targeted area under the pressure at the focus spot we used for sono-chemogenetics (Extended Data Fig. 9c,d).

Although mice are smaller, cheaper and available with more transgenic types for neuroscience research, rats are paramount to clinical translation because of their thicker skulls and larger depths of brain

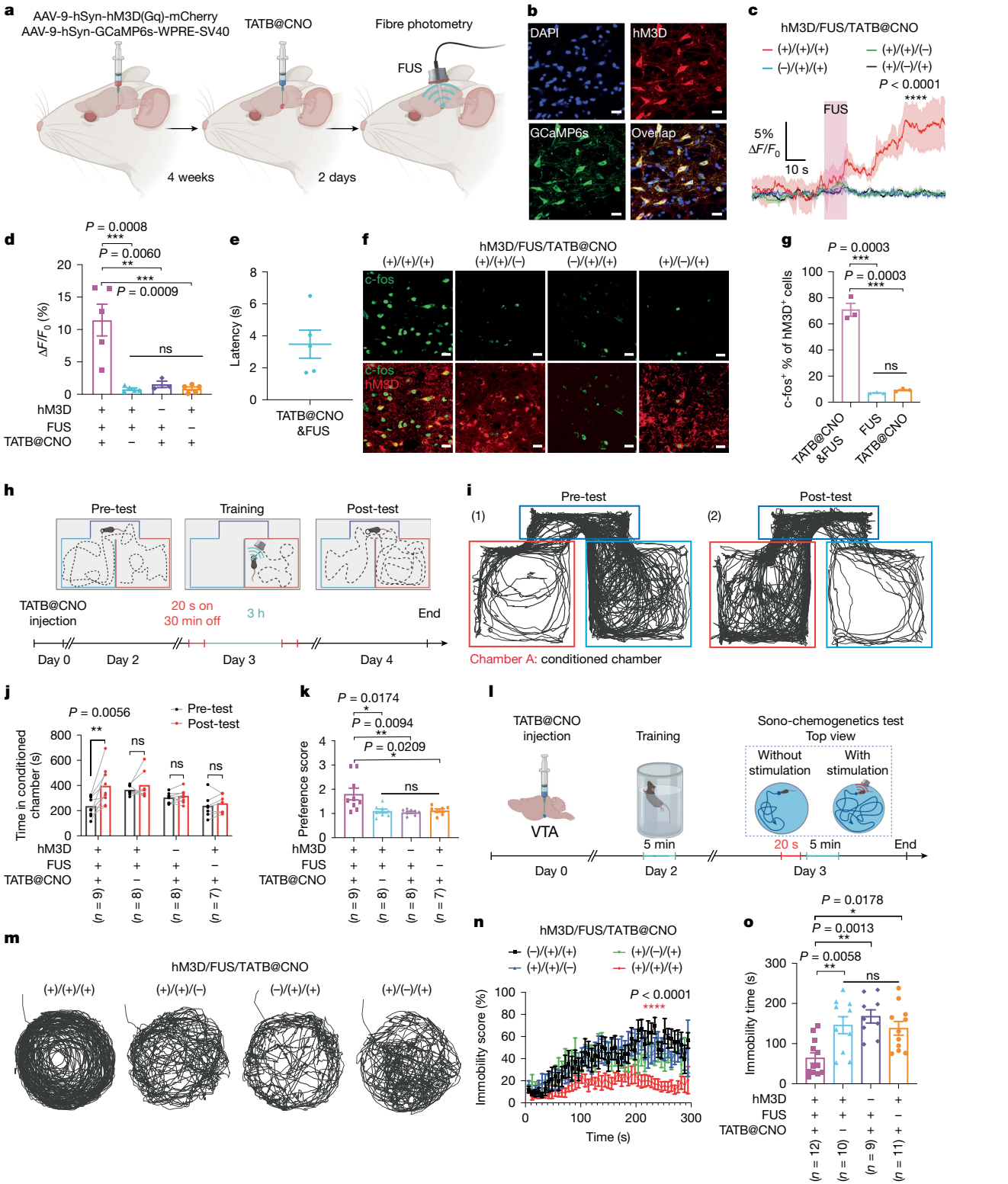

Fig. 4 | In vivo sono-chemogenetic deep brain stimulation in mice. **a**, Experimental scheme of the in vivo fibre photometry in the VTA. **b**, Confocal images showing co-expression of hM3D(Gq) and GCaMP6s in the VTA. Scale bars, 20 µm. $n = 3$ per group. **c**, Normalized GCaMP6s fluorescence change ($\Delta F/F_0$) in mice VTA under different conditions; FUS: 1.5 MHz, 1.40 MPa, pulse 10 s; one-way ANOVA and Tukey's tests. **d**, Statistical analysis of calcium signal changes in **c**; two-way ANOVA and Tukey's tests. Mean ± s.e.m., $n = 5$ (+++), $n = 5$ (++−), $n = 3$ (−++), $n = 5$ (+−+). **e**, Normalized in vivo neuron spiking latency (3.5 s) in mice VTA under sono-chemogenetics. Mean ± s.e.m., $n = 5$. **f**, c-fos expression in the VTA after different treatments (FUS: 1.5 MHz, 1.40 MPa, pulse 20 s, focus 5 mm). Scale bars, 20 µm. $n = 3$ per group. **g**, Quantification of c-fos expression in hM3D(Gq)$^+$ neurons. Mean ± s.e.m., $n = 3$ per condition. Two-way ANOVA and Tukey's tests. **h**, Scheme of CPP tests. **i**, Traces of mouse exploration in CPP apparatus (1) before and (2) after sono-chemogenetics. **j**, Time spent in the FUS stimulation chamber; paired *t*-tests and two-sided comparison test. **k**, CPP preference score; two-way ANOVA and Tukey's tests. Mean ± s.e.m., $n = 9$ (+++), $n = 8$ (++−), $n = 8$ (−++) and $n = 7$ (+−+). **l**, Scheme of FST with sono-chemogenetics. **m**, Representative traces of mice in FST with sono-chemogenetics. **n**, Time-resolved mouse immobility curve in FST. **o**, Statistical analysis of immobility time in FST; mean ± s.e.m., $n = 12$ (+++), $n = 10$ (++−), $n = 9$ (−++), $n = 11$ (+−+); two-way ANOVA and Tukey's tests. Statistical significance: $P \geq 0.05$ (ns), $^*0.01 \leq P < 0.05$, $^{**}0.001 \leq P < 0.01$, $^{***}0.0001 \leq P < 0.001$, $^{****}P < 0.0001$.

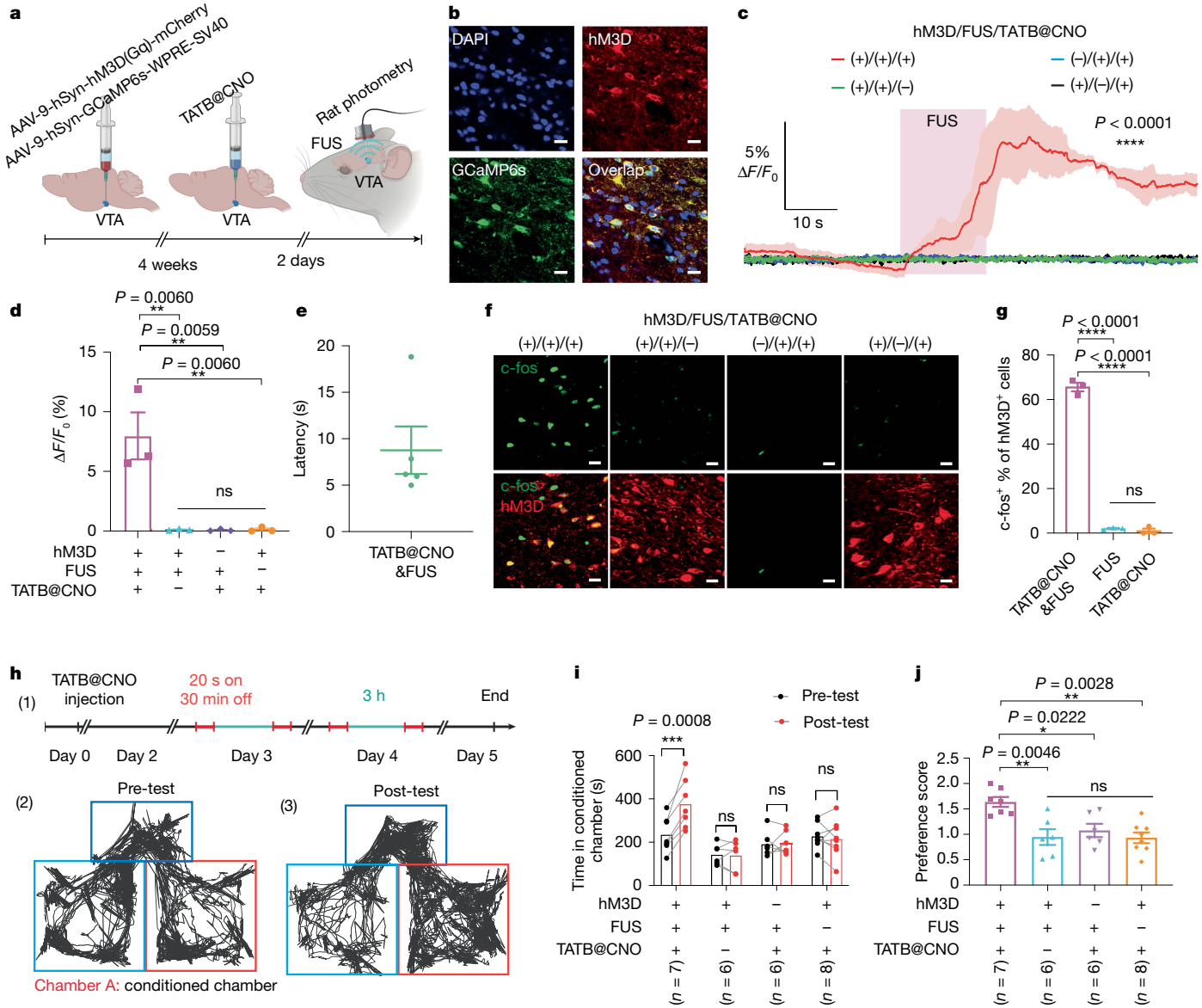

Fig. 5 | In vivo sono-chemogenetic deep brain stimulation in rats. **a**, Experimental scheme of the in vivo fibre photometry in rat VTA. **b**, Confocal images of the co-expression of hM3D(Gq) and GCaMP6s in rat VTA. Scale bars, 20 μm; $n = 3$ independent experiments for each group. **c**, Normalized GCaMP6s fluorescence change ($\Delta F/F_0$) in rat VTA under the different experiment conditions. The pink area represents the FUS irradiation (1.5 MHz, 2.45 MPa, pulse 20 s, focus length 9 mm); solid line, mean; shaded area, s.e.m.; $n = 3$ (+++), $n = 3$ (++−), $n = 3$ (−++), $n = 3$ (+−+); one-way ANOVA and Tukey's tests. **d**, Statistical analysis of calcium signal changes in the rat VTA region under the different conditions. Mean ± s.e.m.; $n = 3$ (+++), $n = 3$ (++−), $n = 3$ (−++), $n = 3$ (+−+); two-way ANOVA and Tukey's tests. **e**, Normalized in vivo neuron spiking latency (8.8 s) in rat VTA under sono-chemogenetics stimulation; mean ± s.e.m.; $n = 5$ represents five independent tests in three rats. **f**, c-fos expression in VTA after the rat is treated with different conditions. Scale bars, 20 μm; $n = 3$ per group. **g**, Quantification of the c-fos expression percentage among the hM3D(Gq)$^+$ neurons; mean ± s.e.m., $n = 3$ per group; two-way ANOVA and Tukey's tests. **h**, Rat CPP tests. (1) Scheme of CPP tests with sono-chemogenetics. Traces of mouse freely exploring apparatus (2) before and (3) after sono-chemogenetic stimulation. **i**, Statistical analysis of time spent in the FUS stimulation chamber; mean ± s.e.m., $n = 7$ (+++), $n = 6$ (++−), $n = 6$ (−++), $n = 8$ (+−+); paired t-tests and two-sided comparison. **j**, Preference score of rats at different conditions; mean ± s.e.m., $n = 7$ (+++), $n = 6$ (++−), $n = 6$ (−++), $n = 8$ (+−+); two-way ANOVA and Tukey's tests. Statistical significance: $P \geq 0.05$ (ns), *$0.01 \leq P < 0.05$, **$0.001 \leq P < 0.01$, ***$0.0001 \leq P < 0.001$, ****$P < 0.0001$.

tissue that more closely meet practical application requirements in the clinic. Minimally invasive, genetically targeted brain modulation has been successfully demonstrated in mice using magnetic nanotransducers[8,36], sonogenetics[40], X-ray-activated systems[41] and near-infrared-based approaches[42]. However, it is still a challenge to achieve genetically targeted deep brain neuromodulation and behaviour control in rats. Using the high energy-transmission efficiency of ultrasound in tissues and the high ultrasound sensitivity of HOF-TATB, we investigated the efficacy of UltraHOF-enabled sono-chemogenetics in rats. Our analysis of the rat head ultrasound heat map showed that a peak ultrasound pressure of 1.19–1.39 MPa was achieved to gate the CNO release, by applying a primary ultrasound power of 2.45 MPa (Extended Data Fig. 9e). Before TATB@CNO nanocrystal injection and optical-fibre implantation, hM3D(Gq) and GCaMP6s were transduced into the rat VTA neurons (Fig. 5a,b). After a recovery period of 2 days, we recorded the green fluorescent signal of GCaMP6s under ultrasound stimulation (1.5 MHz, pulse 20 s, 2.45 MPa) to evaluate the change in neuron activity. We observed a substantial increase in GCaMP6s signal in hM3D(Gq)$^+$ rats with stimulation but not in the absence of hM3D(Gq), TATB@CNO or ultrasound stimulus (Fig. 5c,d). Notably, our UltraHOF-enabled

sono-chemogenetics achieved neuron activation with a latency of 8.8 s from the application of ultrasound and continuous activation for more than 60 s (Fig. 5e). Also, we evaluated neuron activation in post-hoc brain slices by means of c-fos immunostaining. Notable c-fos signals were observed in neurons expressing hM3D(Gq) in the VTA, whereas few c-fos signals were observed in the absence of hM3D(Gq), TATB@CNO or ultrasound stimulus (Fig. 5f,g). These results confirm that our approach can achieve remote brain stimulation even in deep brain regions of rats.

Last, we also assessed the potential of UltraHOF-enabled sono-chemogenetics in shaping behaviours in rats using a 4-day conditioned place preference (CPP) assay. Rats transduced with hM3D(Gq) in the VTA region received TATB@CNO on day 0 and were allowed to freely explore the chambers after a 2-day recovery period. On days 3 and 4, the rats were subjected to ultrasound stimulus (1.5 MHz, pulse 20 s, 2.45 MPa) in the designated conditioned chambers, with two sessions each day. On day 5, post-tests were conducted, in which the rats were allowed to freely explore the chamber without any stimulus (Fig. 5h). The rats treated with our sono-chemogenetics exhibited a preference to stay in the conditioned chamber compared with other groups in post-tests (Fig. 5i). Our results demonstrate a statistically significant difference in the preference score between the hM3D+/FUS+/TATB@CNO+ group and the other control groups without hM3D(Gq), TATB@CNO or ultrasound stimulus (Fig. 5j), indicating that our sono-chemogenetics can effectively modulate reward-learning behaviours in rats through non-invasive deep brain stimulation.

Conclusions

This work presents an ultrasound-activated HOF system with finely tuned interactions at the molecular level through modifying the chemical structure of interaction units. Specifically, HOFs hold together through weak intermolecular hydrogen bond and π−π interactions between each discrete organic molecule unit to form 3D porous frameworks, hence giving them tunable stability in aqueous conditions, high loading capacity and ultrasound-programmable dissociation. Ultrasound stress provided the main driving force to programmably shear the intramolecular non-covalent bonds to achieve controlled mechanochemical activation. Through the manipulation of hydrogen bond density and the number of aromatic fused rings in the backbone structures of the organic ligands, a theoretical model is developed to explain the structure and functionality relationships in the HOFs, providing valuable guidelines for the precise and rational design of HOF building units at the molecular level to achieve on-demand and programmable drug activation under a desirable ultrasound pressure.

Given such abilities of HOFs, ultrasound-triggered temporal and programmable drug activation opened a new realm of non-invasive neural control and medical therapy, such as chemogenetic modulation of targeted neural circuits demonstrated in this study. By tuning HOF nanocrystals sensitivity to respond to FUS, we successfully achieve spatiotemporal control of deep brain neural circuits in both mice and rats with a latency of only seconds. The results demonstrate that UltraHOF-enabled sono-chemogenetics can achieve a high temporal resolution and long-period neuromodulation while retaining the benefits of minimal invasiveness. Our findings have demonstrated that our UltraHOF technology has the combination of high drug-loading content, high biostability, low immunogenicity and unique ultrasound programmability for non-invasive, precise medication therapy. As well as its application for sono-chemogenetics, the UltraHOF technology is capable of releasing different types of molecule with designable medication activation sensitivity and resolution. This enables precise and non-invasive control of various cellular events in deep tissues. We anticipate that this research could serve as a source of inspiration for precise and non-invasive molecular manipulation techniques, potentially applicable in programming molecular robots to achieve sophisticated control over cellular events in deep tissues.

Online content

Any methods, additional references, Nature Portfolio reporting summaries, source data, extended data, supplementary information, acknowledgements, peer review information; details of author contributions and competing interests; and statements of data and code availability are available at https://doi.org/10.1038/s41586-024-08401-0.

1. Huo, S. et al. Mechanochemical bond scission for the activation of drugs. *Nat. Chem.* **13**, 131–139 (2021).
2. Chen, L., Nixon, R. & De Bo, G. Force-controlled release of small molecules with a rotaxane actuator. *Nature* **628**, 320–325 (2024).
3. Rwei, A. Y. et al. Ultrasound-triggered local anaesthesia. *Nat. Biomed. Eng.* **1**, 644–653 (2017).
4. Wang, J. B., Aryal, M., Zhong, Q., Vyas, D. B. & Airan, R. D. Noninvasive ultrasonic drug uncaging maps whole-brain functional networks. *Neuron* **100**, 728–738.e7 (2018).
5. Boulatov, R. The liberating force of ultrasound. *Nat. Chem.* **13**, 112–114 (2021).
6. Suslick, K. S. Sonochemistry. *Science* **247**, 1439–1445 (1990).
7. Mirvakili, S. M. & Langer, R. Wireless on-demand drug delivery. *Nat. Electron.* **4**, 464–477 (2021).
8. Sebesta, C. et al. Subsecond multichannel magnetic control of select neural circuits in freely moving flies. *Nat. Mater.* **21**, 951–958 (2022).
9. Bhansali, D. et al. Nanotechnology for pain management: current and future therapeutic interventions. *Nano Today* **39**, 101223 (2021).
10. Duan, X. et al. Smart pH-sensitive and temporal-controlled polymeric micelles for effective combination therapy of doxorubicin and disulfiram. *ACS Nano* **7**, 5858–5869 (2013).
11. Deisseroth, K. Optogenetics: 10 years of microbial opsins in neuroscience. *Nat. Neurosci.* **18**, 1213–1225 (2015).
12. Bar-Zion, A. et al. Acoustically triggered mechanotherapy using genetically encoded gas vesicles. *Nat. Nanotechnol.* **16**, 1403–1412 (2021).
13. Wang, C. et al. Ultrasound-responsive low-dose doxorubicin liposomes trigger mitochondrial DNA release and activate cGAS-STING-mediated antitumour immunity. *Nat. Commun.* **14**, 3877 (2023).
14. Yao, Y. et al. Remote control of mechanochemical reactions under physiological conditions using biocompatible focused ultrasound. *Proc. Natl Acad. Sci. USA* **120**, e2309822120 (2023).
15. Airan, R. D. et al. Noninvasive targeted transcranial neuromodulation via focused ultrasound gated drug release from nanoemulsions. *Nano Lett.* **17**, 652–659 (2017).
16. Chen, H. & Hwang, J. H. Ultrasound-targeted microbubble destruction for chemotherapeutic drug delivery to solid tumors. *J. Ther. Ultrasound* **1**, 10 (2013).
17. Kiessling, F. et al. Recent advances in molecular, multimodal and theranostic ultrasound imaging. *Adv. Drug Deliv. Rev.* **72**, 15–27 (2014).
18. Shi, Z., Wu, J., Song, Q., Göstl, R. & Herrmann, A. Toward drug release using polymer mechanochemical disulfide scission. *J. Am. Chem. Soc.* **142**, 14725–14732 (2020).
19. Cravotto, G., Gaudino, E. C. & Cintas, P. On the mechanochemical activation by ultrasound. *Chem. Soc. Rev.* **42**, 7521–7534 (2013).
20. Huo, S. et al. Mechano-nanoswitches for ultrasound-controlled drug activation. *Adv. Sci.* **9**, e2104696 (2022).
21. Ghanem, M. A. et al. The role of polymer mechanochemistry in responsive materials and additive manufacturing. *Nat. Rev. Mater.* **6**, 84–98 (2021).
22. Akbulatov, S. et al. Experimentally realized mechanochemistry distinct from force-accelerated scission of loaded bonds. *Science* **357**, 299–303 (2017).
23. Li, J., Nagamani, C. & Moore, J. S. Polymer mechanochemistry: from destructive to productive. *Acc. Chem. Res.* **48**, 2181–2190 (2015).
24. Chen, Y., Mellot, G., van Luijk, D., Creton, C. & Sijbesma, R. P. Mechanochemical tools for polymer materials. *Chem. Soc. Rev.* **50**, 4100–4140 (2021).
25. Wu, M.-X. & Yang, Y.-W. Metal–organic framework (MOF)-based drug/cargo delivery and cancer therapy. *Adv. Mater.* **29**, 1606134 (2017).
26. Bhunia, S., Deo, K. A. & Gaharwar, A. K. 2D covalent organic frameworks for biomedical applications. *Adv. Funct. Mater.* **30**, 2002046 (2020).
27. Lin, R.-B. et al. Multifunctional porous hydrogen-bonded organic framework materials. *Chem. Soc. Rev.* **48**, 1362–1389 (2019).
28. Li, Y.-L. et al. Record complexity in the polycatenation of three porous hydrogen-bonded organic frameworks with stepwise adsorption behaviors. *J. Am. Chem. Soc.* **142**, 7218–7224 (2020).
29. Wang, B. et al. A novel mesoporous hydrogen-bonded organic framework with high porosity and stability. *Chem. Commun.* **56**, 66–69 (2019).
30. Yin, Q. et al. An ultra-robust and crystalline redeemable hydrogen-bonded organic framework for synergistic chemo-photodynamic therapy. *Angew. Chem.* **130**, 7817–7822 (2018).
31. Zentner, C. A. et al. High surface area and *Z*′ in a thermally stable 8-fold polycatenated hydrogen-bonded framework. *Chem. Commun.* **51**, 11642–11645 (2015).
32. Boesmans, W., Hao, M. M. & Vanden Berghe, P. Optogenetic and chemogenetic techniques for neurogastroenterology. *Nat. Rev. Gastroenterol. Hepatol.* **15**, 21–38 (2018).
33. Gomez, J. L. et al. Chemogenetics revealed: DREADD occupancy and activation via converted clozapine. *Science* **357**, 503–507 (2017).
34. Alexander, G. M. et al. Remote control of neuronal activity in transgenic mice expressing evolved G protein-coupled receptors. *Neuron* **63**, 27–39 (2009).

35. Guettier, J.-M. et al. A chemical-genetic approach to study G protein regulation of β cell function in vivo. *Proc. Natl Acad. Sci. USA* **106**, 19197–19202 (2009).
36. Rao, S. et al. Remotely controlled chemomagnetic modulation of targeted neural circuits. *Nat. Nanotechnol.* **14**, 967–973 (2019).
37. Tye, K. M. et al. Dopamine neurons modulate neural encoding and expression of depression-related behaviour. *Nature* **493**, 537–541 (2013).
38. Meng, Y., Hynynen, K. & Lipsman, N. Applications of focused ultrasound in the brain: from thermoablation to drug delivery. *Nat. Rev. Neurol.* **17**, 7–22 (2021).
39. Wang, W. et al. Ultrasound-triggered in situ photon emission for noninvasive optogenetics. *J. Am. Chem. Soc.* **145**, 1097–1107 (2023).
40. Duque, M. et al. Sonogenetic control of mammalian cells using exogenous Transient Receptor Potential A1 channels. *Nat. Commun.* **13**, 600 (2022).
41. Matsubara, T. et al. Author Correction: Remote control of neural function by X-ray-induced scintillation. *Nat. Commun.* **13**, 1950 (2022).
42. Wu, X. et al. Tether-free photothermal deep-brain stimulation in freely behaving mice via wide-field illumination in the near-infrared-II window. *Nat. Biomed. Eng.* **6**, 754–770 (2022).

Methods

HOF nanocrystals preparation

HOF-TATB nanocrystals. 30 mg H_3TATB was dissolved in 3 ml of dimethylformamide (DMF) and then 12 ml of distilled water was added with a stirring speed of 1,000 rpm. After stirring for 10 min, the products were collected by means of centrifugation at 12,000 rpm (13,523 × g) for 5 min (Centrifuge 5420, Eppendorf) and then washed with acetone and distilled water three times, respectively. The final products with around 30% yield were dispersed in water at the desired concentration for future use, in which the concentration was determined through the UV-Vis calibration curve of H_3TATB solution.

HOF-BTB nanocrystals. 30 mg H_3BTB was dissolved in 2 ml of DMF and then 12 ml of distilled water was added with stirring. After 5 min of stirring, the products were collected by centrifugation for 5 min at 12,000 rpm (13,523 × g) and washed with methanol and water three times, respectively. The yield was around 25%.

HOF-101 nanocrystals. Briefly, 30 mg H_4TBAPy was dissolved in 3 ml of DMF and then dropwise added into 12 ml of distilled water with stirring at 1,000 rpm. After 5 min of stirring, the products were separated by centrifugation at 12,000 rpm (13,523 × g) for 5 min and then washed with acetone, ethanol and distilled water three times, respectively. The final products (yield: 95%) were resuspended with distilled water at the desired concentration for future use.

HOF-102 nanocrystals. 10 mg H_4PTTNA monomer was dissolved in 2 ml of DMF and then 8 ml of methanol was added with stirring. After stirring for 5 min, the products were collected by centrifugation for 5 min at 12,000 rpm (13,523 × g) and washed with methanol and water three times, respectively, with a yield of 85%.

Single-crystal structures of HOF-TATB were determined by electron diffraction

Sample preparation. Grains of HOF-TATB in methanol were placed on a Lacey Carbon copper grid (300 mesh). The methanol was evaporated at room temperature and the grid was clipped. The TEM grid was flash frozen in liquid nitrogen. The frozen grid was placed into the autoloader cartridge of the Glacios microscope (Thermo Fisher Scientific) under liquid nitrogen. MicroED data were collected in a Glacios TEM (operating voltage 200 keV, wavelength 0.025 Å), equipped with a Ceta-D CMOS camera (Thermo Fisher Scientific).

MicroED data collection. Crystals were identified in low-magnification search mode and selected for diffraction screening so that they were well separated from other crystals and grid bars. Diffraction of these crystals was tested by acquiring a still diffraction frame by switching the microscope into diffraction mode using the 50-µm C2 aperture and a preset camera length of 0.67. Once a suitable crystal was detected, the microscope was moved back into imaging mode and the maximum tilt range for data collection of the crystal was explored. MicroED data collection was controlled through the programme EPU-D (Thermo Fisher Scientific). Data were collected by continuously rotating the crystal in the beam as the camera acquired diffraction frames (1° s^{-1}) over a tilt range of 50° to 100°. Diffraction data were recorded in rolling shutter mode (0.5 s integration per frame, binned by 2).

Data processing and structure determination. Datasets were indexed, integrated and scaled using the software XDS[43,44]. Diffraction data from several crystals were merged to obtain an almost complete diffraction dataset. The structure of HOF-TATB was determined by ShelXT[45] using direct methods. The dataset was solved in space group P2/c. All non-hydrogen atom locations were identified in the asymmetric unit, and atom types were assigned through chemical knowledge. The structure was refined using ShelXL[46] and the ShelXle[46] and Olex2 (ref. 47) software for viewing and manipulating the structure during refinement. All non-hydrogen atoms were refined anisotropically by full matrix least squares. All hydrogen atoms were placed using a riding model. Refinement statistics can be found in Supplementary Table 4. The structure was deposited at the Cambridge Crystallographic Data Centre under deposition no. CCDC 2338302.

FUS-controlled scission of HOFs. Briefly, 2 ml of fresh HOFs solution was loaded in glass vials and placed on the surface of a FUS transducer (Del Piezo DL-47 and Image Guided Therapy System). Ultrasound peak pressure was determined through a hydrophone (Onda Corporation, HGL-0200) connected to a preamplifier (Onda Corporation, AG-2010) with a gain of 20 dB. The HOFs solution was irradiated under the FUS stimulation with different parameters. After that, 100 µl of solution was extracted at a fixed time and centrifuged at 8,000 rpm for 5 min (Centrifuge 5430, Eppendorf), during which the dissociated monomers or oligomers were separated and mainly located in the supernatant. The supernatant was extracted to carry out the UV-Vis tests (Eppendorf BioSpectrometer basic spectrophotometer) to determine the HOF dissociation percentage according to the following formula:

$$\text{HOFs dissociation percentage} = \frac{\text{Absorption of supernatant}}{\text{Absorption of initial HOFs solution}} \times 100\%$$

Theoretical calculation of the cohesive energy of HOFs and prediction model building. DFT calculations were performed using the Vienna Ab initio Simulation Package[48,49]. Core electrons are described within the projected augmented wave framework; valence electrons are described with a plane-wave basis set up to an energy cutoff of 400 eV (ref. 50). The generalized gradient approximation in the form of the Perdew, Burke and Ernzerhof functional is used to model electronic exchange and correlation. van der Waals interactions are calculated using the DFT-D2 method[51]. Solvation energies are calculated using the VASPsol implicit solvation model[52].

For each HOF, an OMBU is isolated from the crystal structure and optimized to find its energy, E_{mono}. The crystal structures are used to calculate the energy of the HOF, E_{HOF}, except for BTB, in which a fraction of the experimental crystal structure is used as an approximation.

The dissociation of the HOF is modelled as the reaction in equation (1), in which an OMBU breaks away from the bulk HOF state and becomes a dissociated dissolved OMBU.

$$\text{OMBU}_{HOF}(s) \rightarrow \text{OMBU}(aq) \quad (1)$$

Given the experimentally measured dissociation percentage, x, at equilibrium, the dissociation equilibrium constant can be calculated using equation (2):

$$k = \frac{x}{1-x} \quad (2)$$

The cohesive energy $E_{cohesive}$ of each HOF in an aqueous environment is calculated using equation (3):

$$E_{cohesive} = E_{HOF} - nE_{dm} \quad (3)$$

in which E_{HOF} is the energy for a unit cell of the HOF, n is the number of OMBUs in the unit cell and E_{dm} is energy of a dissociated OMBU. For the crystal structures used in this study, n are 8, 2, 2 and 2 for HOF-TATB, HOF-BTB, HOF-101 and HOF-102, respectively.

To characterize the hydrogen-bonding energy E_{HB} and π−π interaction energy $E_{π\text{-}π}$ between two OMBUs, a dimer bonded through hydrogen bonding or π−π interaction is isolated from the crystal structure. The energy of the relaxed dimer is $E_{dimer\text{-}HB}$ and $E_{dimer\text{-}π\text{-}π}$ for

the hydrogen-bonded dimer and the π–π-bonded dimer, respectively. They are used to calculate E_{HB} and $E_{\pi\text{-}\pi}$ using equations (4) and (5):

$$E_{HB} = E_{dimer-HB} - 2E_{dm} \quad (4)$$

$$E_{\pi-\pi} = E_{dimer-\pi-\pi} - 2E_{dm} \quad (5)$$

It is worth noting that E_{HB} is the energy per hydrogen-bonded dimer. One HOF-TATB OMBU can form 2.5 hydrogen bonds, whereas one HOF-101 OMBU can form four hydrogen bonds. Therefore, the total amount of hydrogen-bonding energy an OMBU can have is $1.25E_{HB}$ for HOF-TATB and $2E_{HB}$ for HOF-101.

Structures of the dissociated OMBUs, hydrogen-bonded dimers and π–π-bonded dimers are shown in Supplementary Table 3.

Preparation of drug-loaded HOF nanocrystals. 2 mg of rhodamine B (RB) or CNO was dissolved in 2 ml of a 5 mg ml^{-1} HOF-TATB or other HOF nanocrystal solution. The mixtures were vibrated at 40 °C for 2 h and then centrifuged at 12,000 rpm (13,523 × g) for 5 min. The pellets were washed three times with distilled water to remove unloaded cargoes and then suspended in phosphate-buffered saline (PBS). A 1-ml solution of nanocrystals was extracted for freeze-drying. Subsequently, the resulting powder (1 mg) was dissolved in 1 ml of water (pH 13) to completely release the cargo. The drug-loading content was then measured using UV-Vis spectroscopy.

In vitro ultrasound-controlled drug uncaging. A solution of fresh drug-loaded HOF nanocrystals at a concentration of 1 mg ml^{-1} was loaded into glass vials and positioned on the ultrasound transducer. The solution was irradiated with FUS at a frequency of 1.5 MHz for a specific duration and under desired parameters. At predetermined time intervals, 100 µl of the solution was extracted and centrifuged at 8,000 rpm (6,010 × g) for 5 min. The released drugs were found in the supernatant and the percentage of drug release was calculated using UV-Vis spectroscopy.

Long-term drug stability evaluation in HOF nanocrystals. Drug-loaded HOF nanocrystals at a concentration of 1 mg ml^{-1} were placed in glass vials and stored at room temperature. At specified time intervals, 100 µl of the solution was withdrawn and subjected to centrifugation at 8,000 rpm (6,010 × g) for 5 min. The released drugs were detected in the supernatant and the drug release percentage was determined using UV-Vis spectroscopy.

In vitro calcium imaging. Calcium imaging was performed using primary cortical neurons that were transduced with AAV-9-hSyn-hM3D(Gq)-mCherry and pAAV-hSyn-GCaMP6s-WPRE-SV40. After 6 days of transduction, the neurons were fixed on a fluorescence microscope. The water balloon member of the FUS transducer was brought into contact with the neuron culture medium on top of the plate. Fresh TATB@CNO nanocrystals with a final concentration of 5 µg ml^{-1} CNO were added to the medium. Subsequently, FUS stimulation (1.08 MPa, 1.5 MHz, 10 s duration) was applied to trigger the release of CNO for neuron activation. Imaging videos were captured using a Leica DMi8 fluorescence microscope equipped with a 20× air objective, with a 5-ms exposure time and green channel (Ex: 450–490 nm). The transient increase in green fluorescence ($\Delta F/F$) was calculated by extracting the fluorescence time-series data of 100 neurons through manual segmentation and conversion of the video into greyscale using ImageJ software. The raw data were then processed using a custom MATLAB algorithm that detrends and normalizes the fluorescent time-series data through second-order polynomial curve fits and baseline maximum fluorescent value extraction, compensating for photobleaching effects.

Animal experiments. All procedures were designed according to the National Institutes of Health Guide for the Care and Use of Laboratory Animals, approved by the Institutional Animal Care and Use Committee at the University of Texas at Austin (AUP-2021-00086, AUP-2021-00162 and AUP-2024-00150) and were supported by the Animal Resources Center at the University of Texas at Austin. All of the surgery tools were sterilized before the experiments. Mice and rats were housed in a facility with a 12-h light–dark cycle and provided unrestricted access to both food and water. The housing facility was maintained at 21–24 °C and kept at 40–60% humidity.

Stereotaxic injection of virus. Hair was shaved before the injection and the skin on the head was sterilized three times with 80% ethanol and iodophor. All of the virus injections were conducted by means of the microinjection system (World Precision Instruments, UMP3 Microinjection Syringe Pump) at a rate of 300 nl min^{-1}. After the injection, the needles remained inside the brain for at least 5 min to ensure efficient diffusion of the virus and then it was slowly withdrawn in 5 min. The skin was closed with sutures after the injections. After the surgery, the animals were placed on a 37 °C heating pad and returned to their cage until fully recovered.

Mouse model. C57BL/6 mice (20–26 g; 12–16 weeks old; Jackson Laboratory) were used in our research. Mice were anaesthetized with 2.5% isoflurane using anaesthesia machine (Vaporizer Sales and Service) and the head was fixed in a stereotaxic frame (Kopf Stereotaxic Instruments). Each animal received a subcutaneous injection of meloxicam (5 mg kg^{-1}) and Ethiqa (3.25 mg kg^{-1}) and ophthalmic ointment was used to cover the eyes before surgery. For the photometry tests, 1,200 nl of AAV-9-hSyn-hM3D(Gq)-mCherry (100 µl at titre ≥ 1×10^{13} vg ml^{-1}) and pAAV-hSyn-GCaMP6s-WPRE-SV40 (100 µl at titre ≥ 1×10^{13} vg ml^{-1}) mixture were unilaterally injected into the VTA, with the coordinates relative to the bregma: anteroposterior (AP) −3.08 mm, mediolateral (ML) +0.40 mm and dorsoventral (DV) −5.0 mm (refs. 36,42). Of note, for the behaviour tests, 1,000 nl of AAV-9-hSyn-hM3D(Gq)-mCherry solution was unilaterally injected into the VTA. After 4 weeks, these mice were used for experiments.

Rat model. 3–4-month-old Long–Evans rats (Charles River) were used in our experiments. Rats were anaesthetized with 5% isoflurane and received a subcutaneous injection of meloxicam (2 mg kg^{-1}) and Ethiqa (0.65 mg kg^{-1}) before surgery. For the photometry tests, 1,200 nl of AAV-9-hSyn-hM3D(Gq)-mCherry and pAAV-hSyn-GCaMP6s-WPRE-SV40 mixture were unilaterally injected into the VTA, with the coordinates relative to bregma: −5.0 mm AP, +1.0 mm ML and −8.6 mm DV (ref. 53). For the behaviour tests, 1,000 nl of AAV-9-hSyn-hM3D(Gq)-mCherry was unilaterally injected into the VTA. After 4 weeks, these rats could be used for experiments.

Mouse photometry tests. The hM3D(Gq) and GCaMP6s transduced mice were used for the photometry tests. 2 µl of TATB@CNO (2 mg ml^{-1}) nanocrystals were unilaterally injected into the VTA with the same coordinates as the viral injection. Then, the optical fibres were implanted at the virus-transduced VTA area (−3.08 mm AP, +0.5 mm ML, −5.0 mm DV). After recovery for 2 days, the mouse head was head-fixed and FUS (1.5 MHz, 1.40 MPa, 10 s duration) was used to irradiate the VTA area. The FUS focus length was set to be 5 mm through control of the FUS water bubble. The signal was recorded through the R810 Dual Color Multichannel Fiber Photometry System (RWD Life Science)[54].

Mouse FST evaluation. hM3D(Gq) transduced mice (20–24 weeks old) were used. A cylindrical tank (20 cm diameter, 30 cm height) was used for mice FST. The water level was around 15 cm and the water temperature was around 23–25 °C (ref. 55). The cylindrical tank was surrounded by a white background when we were ready to carry out the tests. On day 0, 2 µl of TATB@CNO (2 mg ml^{-1}) nanocrystals were unilaterally injected into the VTA (−3.08 mm AP, +0.5 mm ML, −5.0 mm DV). After 2 days of recovery, the mouse was subjected to a 5-min pre-test without FUS stimulation on day 2. On day 3, FUS (1.5 MHz, 1.40 MPa, 20 s duration) was used to irradiate the VTA area through control of the FUS focus length (−3.08 mm AP, +0.5 mm ML, −5.0 mm DV). After that, the mouse was placed in the FST container and 5-min FST videos were recorded to analyse the immobility. Trajectory data were obtained from pre-built software integrated into the recorded FST videos using

the R820 Tricolor Multichannel Fiber Photometry System (RWD Life Science). A custom-made algorithm in MATLAB was developed for FST data analysis. The difference in position between subsequent frames of the video was used to determine the displacement of the mice, which was then divided by the frames per second of the video to determine the velocity. A threshold value of the velocity of 0.1 pixels s^{-1} was found to be the optimal value for determining the state of mobility and immobility for mice in FST across groups. For every 5-s window, the time accrued between frames during which the velocity is less than the threshold is accumulated and was used as a proportion to the 5-s window to determine the immobility percentage over time. The total immobility time was determined similarly by accumulating the total time during which the velocity between frames was below the threshold.

Mouse CPP tests. After the injection of AAV (AAV-9-hSyn-hM3D(Gq)-mCherry) for 4 weeks, 2 µl of TATB@CNO (2 mg ml^{-1}) nanocrystals were unilaterally injected into the VTA (−3.08 mm AP, +0.5 mm ML, −5.0 mm DV) on day 0. Briefly, the two side boxes (30 cm × 60 cm × 30 cm) were made of plexiglass and conjugated with one medium chamber (15 cm × 30 cm × 30 cm). One side box was covered with white and red striped papers and the other was covered with yellow and blue striped papers[56]. On day 2, the mice were placed in the medium chamber to allow them to freely explore the apparatus for 15 min (pre-test). On day 3, mice were conditioned with two sessions. First, the mice were irradiated with FUS (1.5 MHz, 1.40 MPa, 20 s duration) and then restricted to designated conditioned chambers for 30 min. In the second session around 3 h later, mice received the same treatment and were then restricted to designated conditioned chambers for 30 min. On day 4, the mice were placed and restricted in the medium chamber for 5 min. After that, the mice were allowed to freely move. The videos were recorded through a trail-tracking camera. The data were analysed through the R810 Dual Color Multichannel Fiber Photometry System with a behaviour tracking system (RWD Life Science). For place preference tests, mice was chosen for tests only if the baseline preference for either side chamber is between 10% and 70%, or for the medium chamber is <40% (ref. 56).

Rat photometry tests. hM3D(Gq) and GCaMP6s transduced rats were used. 2 µl of TATB@CNO (10 mg ml^{-1}) nanocrystals were unilaterally injected into the VTA with similar coordinates (−5.0 mm AP, +1.0 mm ML, −8.6 mm DV). Then, the optical fibres were implanted into a similar area. After recovery for 2 days, the rat head was fixed, and FUS (1.5 MHz, 2.45 MPa, 20 s duration) was used to irradiate the VTA area. The FUS focus length was set to 9 mm through control of the FUS water bubble. The signal was recorded through the R810 Dual Color Multichannel Fiber Photometry System (RWD Life Science).

Rat CPP tests. After 4 weeks of expression of hM3D(Gq) in VTA neurons in rats, 2 µl of TATB@CNO (10 mg ml^{-1}) nanocrystals were unilaterally injected into the VTA (−5.0 mm AP, +1.0 mm ML, −8.6 mm DV) on day 0. Similar to mice CPP tests, the two side boxes (30 cm × 60 cm × 30 cm) were made of plexiglass but conjugated with one medium chamber (25 cm × 30 cm × 30 cm). On day 2, the rats were placed in the medium chamber and left to acclimatize for 5 min. After that, we opened the door to allow them to freely explore the apparatus for 15 min (pre-test). On day 3, rats were conditioned with two sessions. First, the rats were irradiated with FUS (1.5 MHz, 2.45 MPa, 20 s duration) and then restricted to designated conditioned chambers for 30 min. In the second session around 3 h later, rats received the same treatment and were then restricted to designated conditioned chambers for 30 min. On day 4, the two pairing sessions were repeated, similar to day 3. After 2 days of training, we started the tests on day 5. The rats were placed and restricted in the medium chamber for 5 min. After that, they were allowed to freely move for 15 min. The data-analysis methods were similar to the mice CPP tests.

c-fos staining in mice/rats brain sections. Specifically, mice/rats expressing hM3D(Gq) in VTA neurons and wild-type mice/rats were first subjected to sono-chemogenetics treatment. After 60 min, the mice/rats were anaesthetized with ketamine (16 mg kg^{-1}) administered intraperitoneally. Following induction of deep anaesthesia, perfusion was performed using PBS, followed by 4% paraformaldehyde. The brains were then extracted and stored in 4% paraformaldehyde at 4 °C overnight and sliced using a vibrating blade microtome (Leica VT1200). Brain slices with a depth of 60 µm were washed with 0.3% Triton-X PBS (TBS) solution and subsequently blocked with 5% bovine serum albumin TBS solution for 30 min at room temperature. In the case of mouse brain sections, following the blocking step, the samples were incubated with rabbit anti-c-Fos antibody (ab222699, Abcam, 1:500)/mouse anti-tyrosine hydroxylase antibody (MA1-24654, Fisher Scientific, 1:1,000)/0.3% Triton-X in PBS. The samples were then incubated at 4 °C overnight and washed three times with TBS solution. Next, a mixture of TBS and secondary antibodies, including goat anti-rabbit Alexa Fluor 405 (ab175652, Abcam, 1:500), goat anti-mouse Alexa Fluor 488 (ab150113, Abcam, 1:1,000) and Hoechst 33342 (17535, ATT Bioquest, 1:5000), was added and the slices were incubated for 2 h at room temperature in a dark room. The slices were then washed three times with TBS, mounted on slides using mounting media (9990402, Fisher Scientific) and covered with a coverslip. Confocal images were obtained using a Zeiss 710 laser scanning microscope. For rat brain sections, the procedure was identical except for the use of rabbit anti-c-Fos antibody (ab289723, Abcam, 1:500) instead of ab222699. Detailed information on the antibodies used in this study can be found in Supplementary Table 10.

Reporting summary

Further information on research design is available in the Nature Portfolio Reporting Summary linked to this article.

Data availability

The code used to analyse the data in this study is available from the GitHub repository for this article (https://github.com/kevintang725/ultrasound-programmable-hydrogen-bonded-organic-frameworks-for-sono-chemogenetics). Crystallographic data for the structures in this article have been deposited at the Cambridge Crystallographic Data Centre under deposition no. CCDC 2338302 (HOF-TATB). Copies of the data can be obtained free of charge from https://www.ccdc.cam.ac.uk/structures/. All other data supporting the findings of this study are available in the article and its Supplementary information and Supplementary Data. Source data are provided with this paper.

43. Pawley, G. S. Unit-cell refinement from powder diffraction scans. *J. Appl. Crystallogr.* **14**, 357–361 (1981).
44. Sheldrick, G. M. Crystal structure refinement with SHELXL. *Acta Crystallogr. C* **71**, 3–8 (2015).
45. Sheldrick, G. M. SHELXT – integrated space-group and crystal-structure determination. *Acta Crystallogr. A* **71**, 3–8 (2015).
46. Hübschle, C. B., Sheldrick, G. M. & Dittrich, B. ShelXle: a Qt graphical user interface for SHELXL. *J. Appl. Crystallogr.* **44**, 1281–1284 (2011).
47. Dolomanov, O. V., Bourhis, L. J., Gildea, R. J., Howard, J. A. K. & Puschmann, H. OLEX2: a complete structure solution, refinement and analysis program. *J. Appl. Crystallogr.* **42**, 339–341 (2009).
48. Kresse, G. & Hafner, J. *Ab initio* molecular dynamics for liquid metals. *Phys. Rev. B* **47**, 558–561 (1993).
49. Kresse, G. & Joubert, D. From ultrasoft pseudopotentials to the projector augmented-wave method. *Phys. Rev. B* **59**, 1758–1775 (1999).
50. Blöchl, P. E. Projector augmented-wave method. *Phys. Rev. B* **50**, 17953–17979 (1994).
51. Grimme, S. Semiempirical GGA-type density functional constructed with a long-range dispersion correction. *J. Comput. Chem.* **27**, 1787–1799 (2006).
52. Sundararaman, R. & Schwarz, K. Evaluating continuum solvation models for the electrode-electrolyte interface: challenges and strategies for improvement. *J. Chem. Phys.* **146**, 084111 (2017).
53. Witten, I. B. et al. Recombinase-driver rat lines: tools, techniques, and optogenetic application to dopamine-mediated reinforcement. *Neuron* **72**, 721–733 (2011).
54. Zan, G.-Y. et al. Amygdalar κ-opioid receptor-dependent upregulating glutamate transporter 1 mediates depressive-like behaviors of opioid abstinence. *Cell Rep.* **37**, 109913 (2021).
55. Can, A. et al. The mouse forced swim test. *J. Vis. Exp* **(59)**, 3638 (2012).
56. Airan, R. D., Thompson, K. R., Fenno, L. E., Bernstein, H. & Deisseroth, K. Temporally precise in vivo control of intracellular signalling. *Nature* **458**, 1025–1029 (2009).

Acknowledgements TEM image acquisition was performed with the help of M. Mikesh at the Center for Biomedical Research Support Microscopy and Imaging Facility at UT Austin (RRID# SCR_021756). H.W. acknowledges funding support from the National Science Foundation (NSF) CAREER award (2340964), NIH Maximizing Investigators' Research Award (National Institute of General Medical Sciences 1R35GM147408), the University of Texas at Austin Startup Fund, Robert A. Welch Foundation Grant (no. F-2084-20210327) and Craig H. Neilsen Foundation Pilot Research Grant. We acknowledge BioRender.com for the figures drawing.

Author contributions W.W. and H.W. designed the project. W.W. led the materials characterization, cell tests, animal tests and their analysis. Y.S., Y.X. and B.C. designed, synthesized and characterized the HOF materials. N.H., W.Z. and D.W.M. performed the electron diffraction tests and crystal analysis. W.H. helped with high-performance liquid chromatography tests. W.C. and G.H. conducted molecular simulation computing and discussed the data. K.W.K.T., I.P., X.L. and X.S. helped W.W. to build animal models and animal behaviour tests. J.J., J.-C.H., A.R.L. and B.A. helped with animal behaviour data analysis and immunohistology tests. B.S., N.B.S. and T.P. conducted the blood–brain barrier opening tests. All of the co-authors contributed to the writing of the manuscript. B.C. and H.W. supervised the project.

Competing interests H.W., W.W., Y.S. and B.C. declare that a patent application (PCT/US2024/042314) relating to this work has been filed. The other authors declare no competing interests.

Additional information

Supplementary information The online version contains supplementary material available at https://doi.org/10.1038/s41586-024-08401-0.

Correspondence and requests for materials should be addressed to Banglin Chen or Huiliang Wang.

Peer review information *Nature* thanks Andrew P. Goodwin and the other, anonymous, reviewer(s) for their contribution to the peer review of this work. Peer reviewer reports are available.

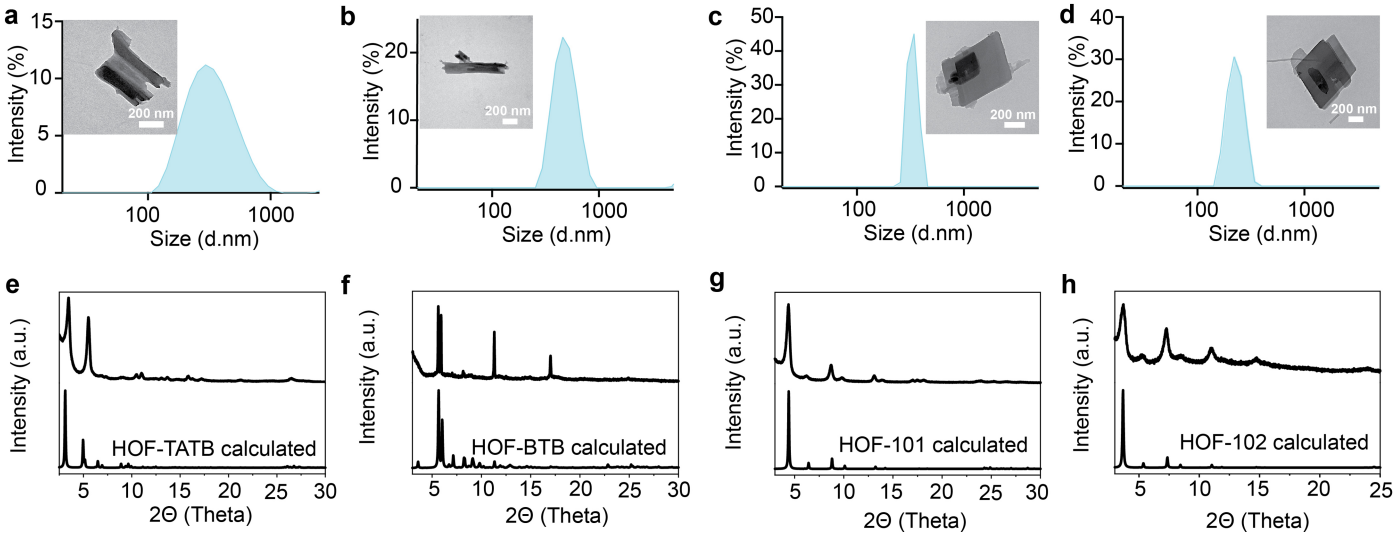

Extended Data Fig. 1 | Morphology, size and crystal structure of all four different HOF nanocrystals that were characterized. a–**d**, TEM images and hydrodynamic size distribution measured by DLS of HOF-TATB nanocrystals (**a**), HOF-BTB nanocrystals (**b**), HOF-101 nanocrystals (**c**) and HOF-102 nanocrystals (**d**). **e**–**h**, The X-ray diffraction tests of HOF nanocrystals: HOF-TATB (**e**), HOF-BTB (**f**), HOF-101 (**g**), HOF-102 (**h**). $n = 3$ independent experiments for each sample.

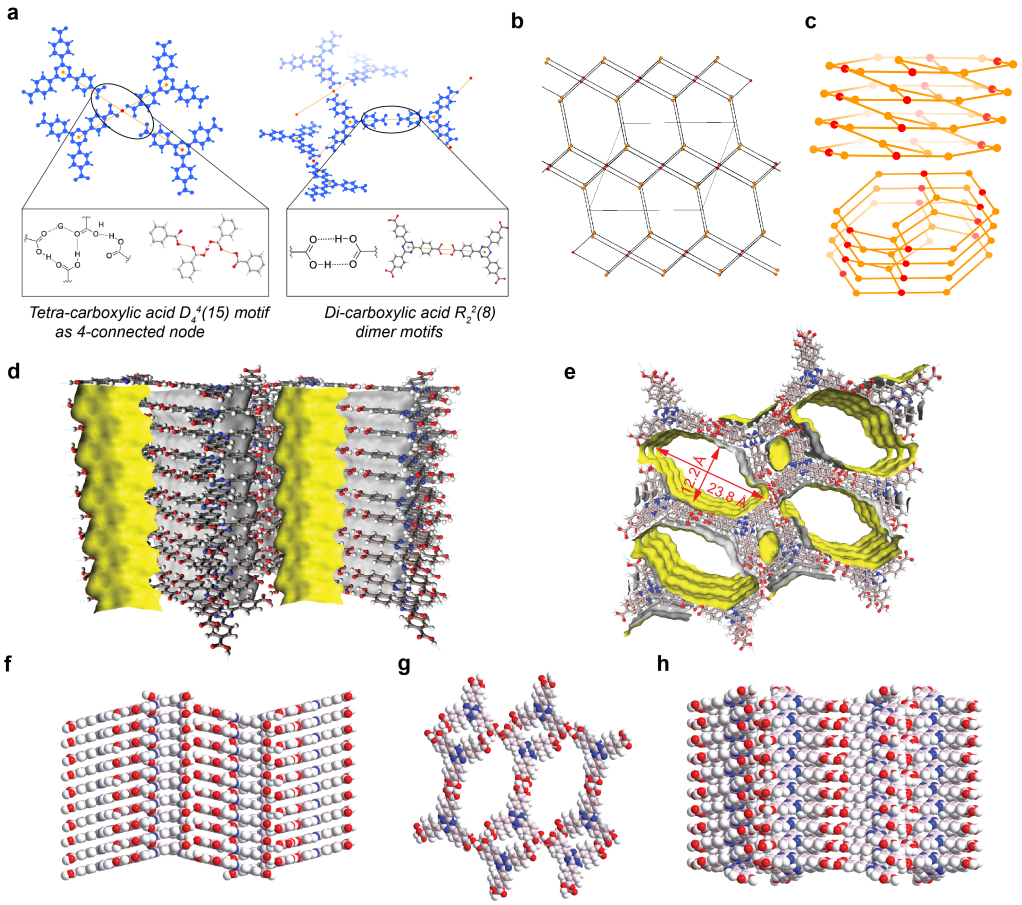

Extended Data Fig. 2 | Topology analysis of HOF-TATB. a, Structures of two different hydrogen-bonding motifs and their simplified forms. **b**, 3D structure of the interpenetrated network in HOF-TATB and its simplified 3,4-connected topology viewed from the *c* axis. **c**, Perspective view of a simplified single net. **d**,**e**, Calculated pore surface of 1D pore channel of HOF-TATB: view along *a* axis (**d**); view along *b* axis (**e**). (Connolly surface with pore radius of 1.2 Å). **f**–**h**, Crystal structure scheme of HOF-TATB: view along *a* axis (**f**); view along *b* axis (**g**); view along *c* axis (**h**).

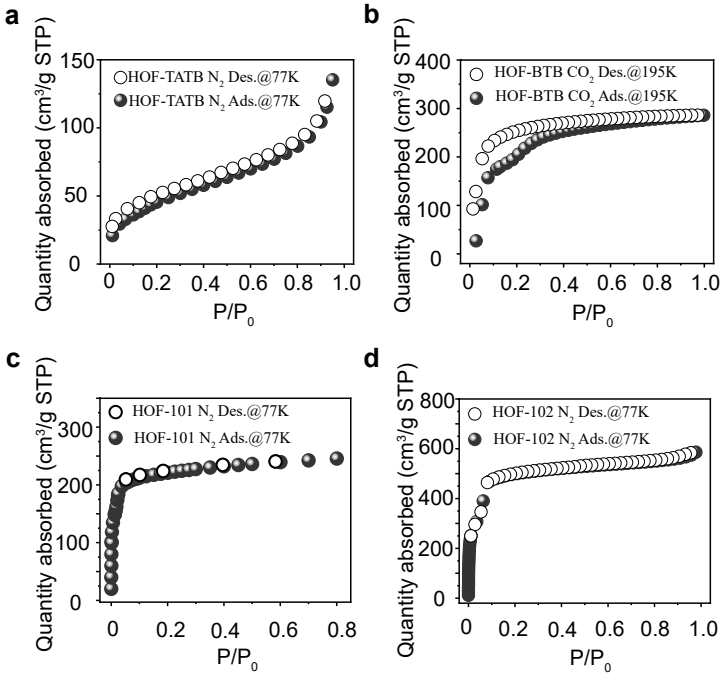

Extended Data Fig. 3 | Porosity characterization of the four different nanocrystals. a, Single-component sorption isotherms of nitrogen at 77 K of HOF-TATB, indicating the framework flexibility. **b**, Single-component sorption isotherms of CO_2 at 195 K of HOF-BTB (no nitrogen adsorption is observed at 77 K), indicating framework flexibility. **c**, Single-component sorption isotherms of nitrogen at 77 K of HOF-101. **d**, Single-component sorption isotherms of nitrogen at 77 K of HOF-102. $n = 3$ independent experiments for each sample.

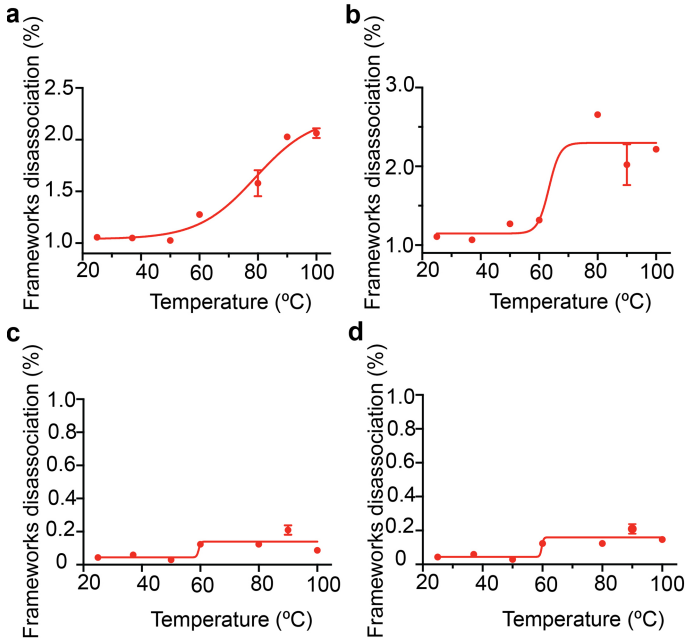

Extended Data Fig. 4 | Thermal dissociation tests of HOF nanocrystals. **a**, HOF-TATB, **b**, HOF-BTB, **c**, HOF-101, **d**, HOF-102. The HOF nanocrystals were incubated at different temperatures for 5 min. After that, the HOFs solution was extracted and centrifuged and the supernatant was used to perform UV-Vis tests for HOFs dissociation determination. The thermal dissociation occurred around 60 °C. Only around a 2% increase was observed at HOF-TATB and HOF-BTB and no thermal dissociation was observed in HOF-101 and HOF-102, at temperature 100 °C. Mean ± s.e.m., $n = 3$ independent experiments for each sample.

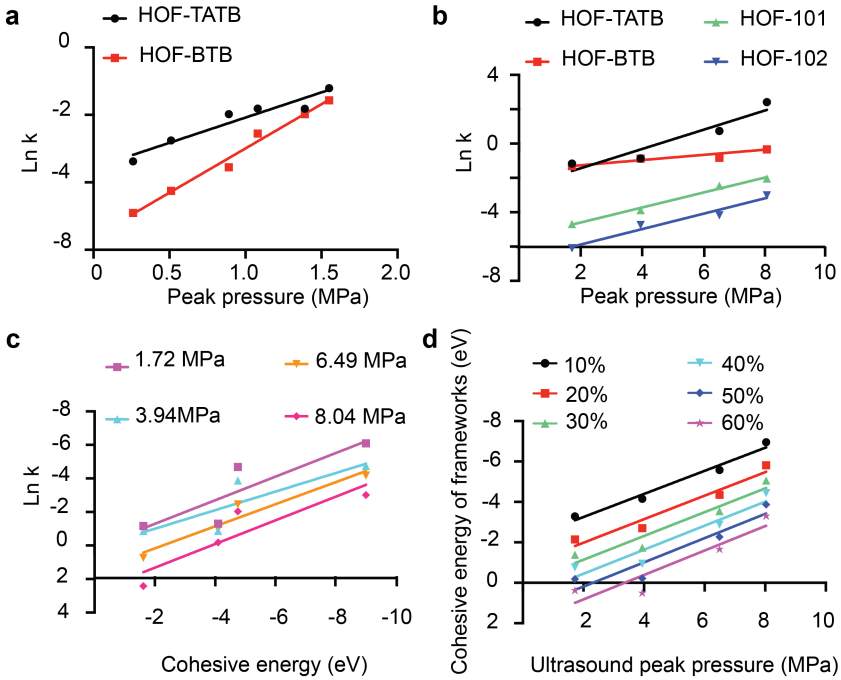

Extended Data Fig. 5 | Theoretical modelling of mechanochemical scission in HOFs. a, A linear model fits the relationship between the ultrasound peak pressure and the ln(k) of HOFs when the peak pressure is less than 1.55 MPa; n = 3 independent experiments for each sample. **b**, A linear model fits the relationship between the ultrasound peak pressure and the ln(k) of HOFs when the peak pressure is up to 1.55 MPa. n = 3 independent experiments for each sample. **c**, A linear model qualitatively fits the relationship between the $E_{cohesive}$ of HOFs and the ln(k) at fixed E_{US}. With 1.72, 3.94, 6.49 and 8.04 MPa peak pressure, ln(k) of HOF-TATB, HOF-BTB, HOF-101 and HOF-102 correlate to their cohesion energy linearly, respectively. n = 3 independent experiments for each sample. **d**, When ln(k) is held constant, a linear correlation is observed between the ultrasound peak pressure and the cohesive energy of HOFs. To achieve a targeted 10%, 20%, 30%, 40%, 50% and 60% dissociation of HOFs at a fixed ultrasound peak pressure, it is possible to calculate the corresponding $E_{cohesive}$ of HOFs using the established linear relationship.

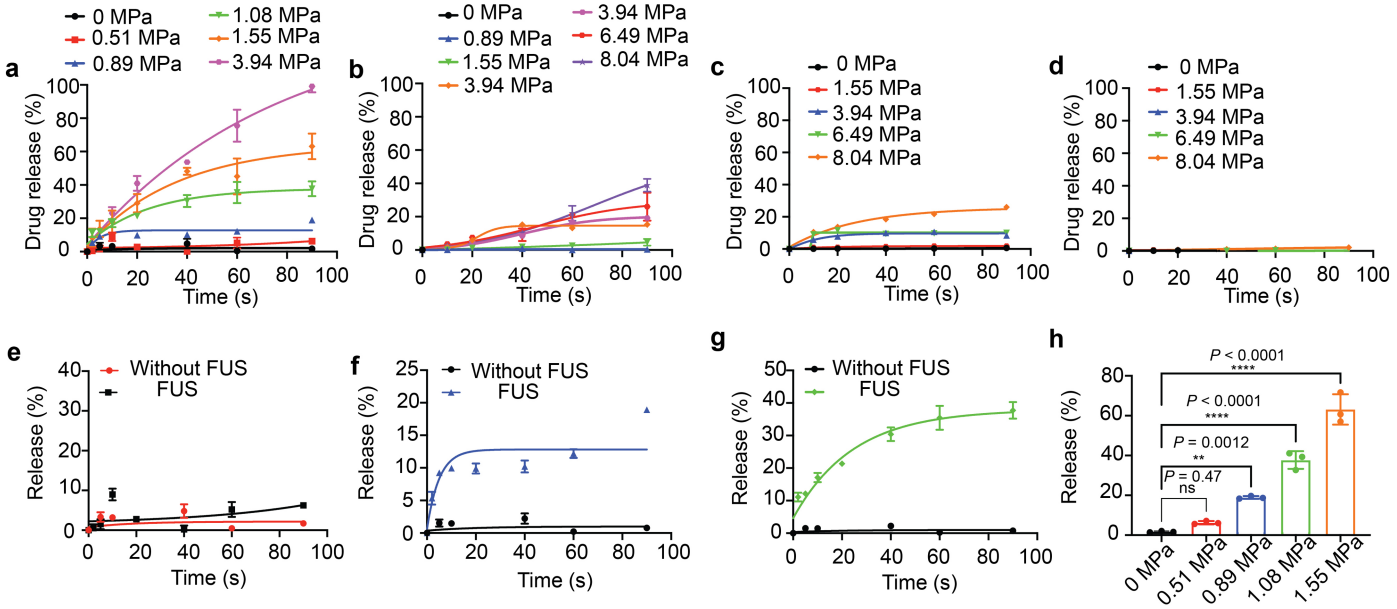

Extended Data Fig. 6 | Ultrasound-triggered drug release from different HOF nanocrystals. a, HOF-TATB. **b**, HOF-BTB. **c**, HOF-101. **d**, HOF-102. The fluorescence dye RB was first loaded into the HOF nanocrystals. After that, the ultrasound irradiated the RB-loaded nanocrystals with different power densities. At fixed time points, the solution was taken out and centrifuged. The released RB concentration was determined through UV-Vis from the supernatant. Mean ± s.e.m., $n = 3$ independent experiments for each sample. **e**–**h**, Ultrasound-triggered drug release from HOF-TATB. The fluorescence dye RB was first loaded into the HOF-TATB nanocrystals (TATB@RB). After that, the TATB@RB nanocrystals were irradiated by the ultrasound with different power densities, including 0.51 MPa (**e**), 0.89 MPa (**f**) and 1.08 MPa (**g**), and the quantification of drug release percentage without ultrasound and with ultrasound for 90 s (**h**). Mean ± s.e.m., $n \geq 3$ independent samples. One-way ANOVA and Dunnett's multiple comparison tests ($P \geq 0.05$ (ns), $^{*}0.01 \leq P < 0.05$, $^{**}0.001 \leq P < 0.01$, $^{****}P < 0.0001$). Mean ± s.e.m., $n = 3$ independent experiments for each sample.

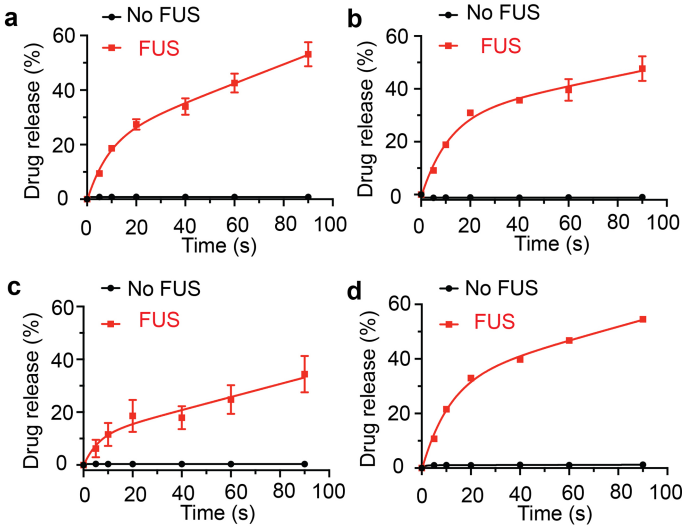

Extended Data Fig. 7 | Ultrasound-triggered release of various drugs. **a**, Deschloroclozapine. **b**, Dopamine. **c**, Procaine. **d**, CNO from HOF-TATB at 1.5 MHz, 1.55 MPa (mean ± s.e.m., $n = 3$ independent samples).

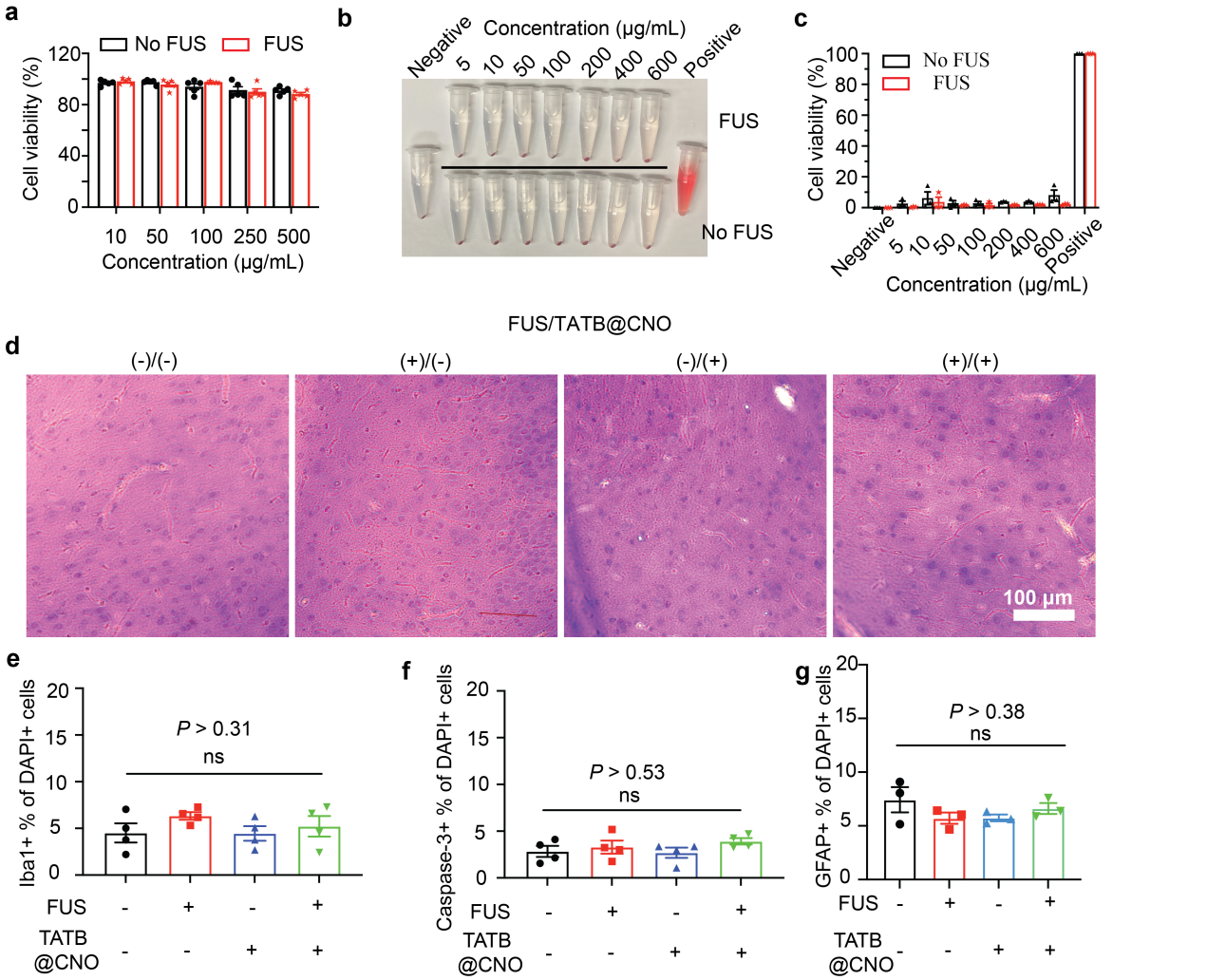

Extended Data Fig. 8 | Biosafety and biocompatibility evaluation of UltraHOF. a, The cell viability tests of HOF-TATB nanocrystals in human embryonic kidney 293 (HEK-293T) cells. Mean ± s.e.m.; at least three independent tests ($n = 5$). The hemolysis tests of HOF-TATB nanocrystals: photograph (**b**) and hemolysis statistical analysis (**c**); mean ± s.e.m.; at least three independent tests ($n \geq 3$). **d**, In vivo biosafety evaluation by haematoxylin and eosin staining after sono-chemogenetics. Scale bar, 100 μm. $n = 3$ independent experiments for each sample. **e**, In vivo biocompatibility evaluation of the sono-chemogenetics by means of determining microglia (Iba1) activation. Statistical analysis of the Iba1 intensity. Mean ± s.e.m., $n \geq 3$ mice in each group. Two-way ANOVA and Tukey's multiple comparison tests. **f**, In vivo biocompatibility evaluation of the sono-chemogenetics by means of determining neuron apoptosis (caspase-3). Statistical analysis of the caspase-3 intensity. Mean ± s.e.m., $n \geq 3$ mice in each group. Two-way ANOVA and Tukey's multiple comparison tests. **g**, In vivo biocompatibility evaluation of the sono-chemogenetics by determining astrocytes (GFAP) activation. Mean ± s.e.m., $n \geq 3$ mice in each group. Two-way ANOVA and Tukey's multiple comparison tests. Statistical significance: $P \geq 0.05$ (ns).

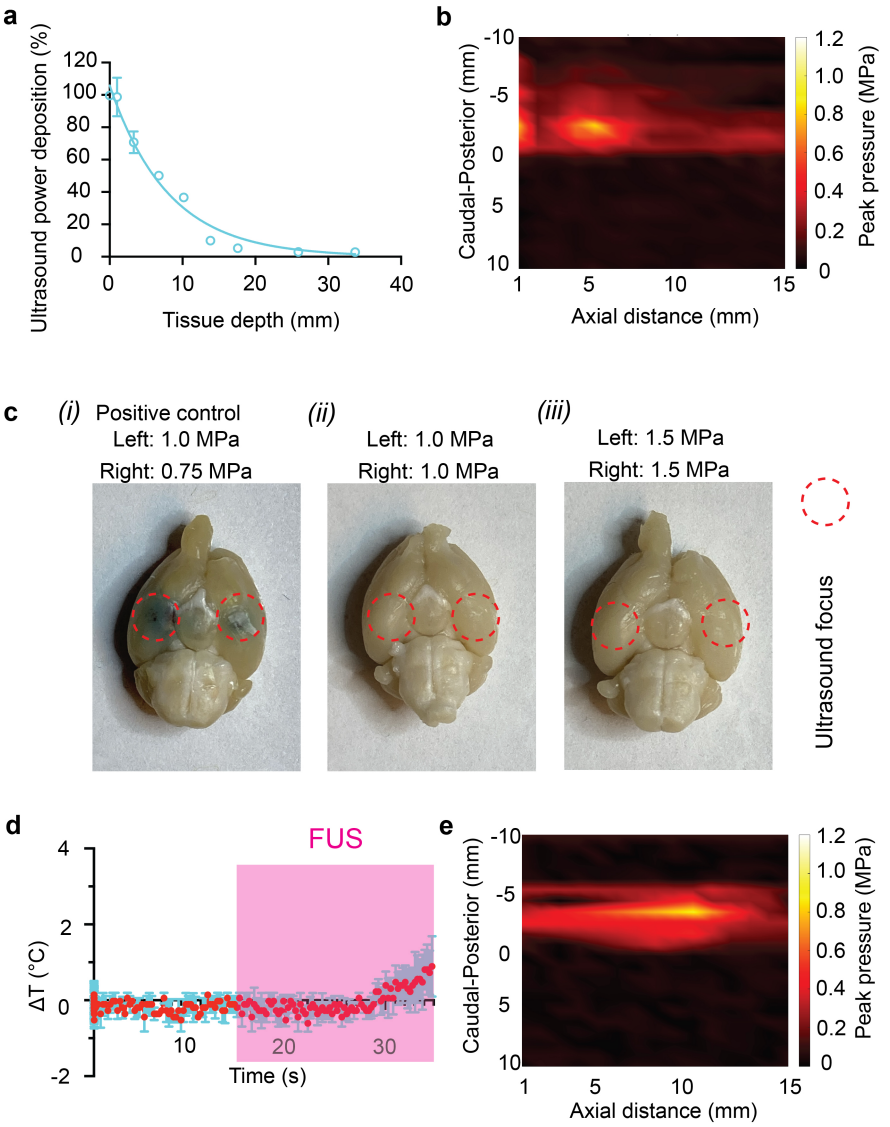

Extended Data Fig. 9 | Ultrasound power delivery in the tissue and biosafety evaluation. a, To measure ultrasound power transfer efficiency through tissue, pork skin of varying depths was placed on a 1.5-MHz, 2.40-MPa FUS transducer. The results showed that 1.5-MHz ultrasound could penetrate up to 20 mm, with a power transfer efficiency of 37% at 10 mm depth; mean ± s.e.m.; $n = 3$. **b**, The in vivo ultrasound power transfer in the mouse head with FUS focus length of 5 mm. The ultrasound peak pressure heat map in the mouse head shows that around 0.90 MPa was delivered to the mouse VTA when 1.40 MPa primary ultrasound peak pressure was used. **c**, Ultrasound-induced blood-brain barrier opening evaluation through Evans blue staining. (i) Brains from mice injected with microbubbles and given 20 s ultrasound at 1.0 MPa (left) and 0.75 MPa (right). (ii) Brains from mice without microbubbles given 20 s ultrasound at 1.0 MPa. (iii) Brains from mice without microbubbles given 20 s ultrasound at 1.5 MPa. Red circles show ultrasound-treated areas. **d**, The evaluation of ultrasound-induced thermal effects at the focus. Real-time temperature detection was conducted at the mice VTA during FUS stimulation (1.5 MHz, 1.55 MPa, duration 20 s). No substantial temperature changes were observed during the initial 10 s of ultrasound exposure, with only a slight increase of approximately 1.25 °C detected after the 20 s stimulus. Mean ± s.e.m., $n = 3$ independent experiments for each sample. **e**, The in vivo ultrasound power transfer in rat heads with FUS focus length of 10 mm. The ultrasound peak pressure heat map in the rat head shows that around 1.19–1.39 MPa was delivered to the rat VTA when 2.45 MPa primary ultrasound peak pressure was used.

nature portfolio

Corresponding author(s): Huiliang Wang, and Banglin Chen

Last updated by author(s): Dec 19, 2023

Reporting Summary

Nature Portfolio wishes to improve the reproducibility of the work that we publish. This form provides structure for consistency and transparency in reporting. For further information on Nature Portfolio policies, see our Editorial Policies and the Editorial Policy Checklist.

Statistics

For all statistical analyses, confirm that the following items are present in the figure legend, table legend, main text, or Methods section.

n/a	Confirmed
☐	☒ The exact sample size (*n*) for each experimental group/condition, given as a discrete number and unit of measurement
☐	☒ A statement on whether measurements were taken from distinct samples or whether the same sample was measured repeatedly
☐	☒ The statistical test(s) used AND whether they are one- or two-sided *Only common tests should be described solely by name; describe more complex techniques in the Methods section.*
☒	☐ A description of all covariates tested
☐	☒ A description of any assumptions or corrections, such as tests of normality and adjustment for multiple comparisons
☐	☒ A full description of the statistical parameters including central tendency (e.g. means) or other basic estimates (e.g. regression coefficient) AND variation (e.g. standard deviation) or associated estimates of uncertainty (e.g. confidence intervals)
☐	☒ For null hypothesis testing, the test statistic (e.g. *F*, *t*, *r*) with confidence intervals, effect sizes, degrees of freedom and *P* value noted *Give P values as exact values whenever suitable.*
☒	☐ For Bayesian analysis, information on the choice of priors and Markov chain Monte Carlo settings
☒	☐ For hierarchical and complex designs, identification of the appropriate level for tests and full reporting of outcomes
☒	☐ Estimates of effect sizes (e.g. Cohen's *d*, Pearson's *r*), indicating how they were calculated

Our web collection on statistics for biologists contains articles on many of the points above.

Software and code

Policy information about availability of computer code

Data collection	In vitro calcium imaging videos were recorded by Leica DMi8. Confocal images were obtained using a Zeiss 710 laser scanning microscope.Bruker 400 MHz Avance III HD Nano was used for collections of 1H NMR spectra (1H NMR, 400 MHz). The powder X-ray diffraction patterns were collected by a Panalytical X'Pert powder diffractometer equipped with a Cu-sealed tube (λ = 1.54184 Å) at 40 kV and 40 mA over the 2θ range of 5–40°. UV-Vis spectra were recorded using an Eppendorf BioSpectrometer Basic. The drug release percentage from HOFs was measured using HPLC (Agilent 6120 Single Quad LC/MS). Microplate reader (BioTek Synergy H1, 560ex/590em nm) was used to measure the cell viability. Mouse movement videos in forced swimming test assays were tracked by R820 Tricolor Multi-Channel Fiber Photometry System, RWD. The animal movement videos in mouse/rat conditioned place preference tests were recorded by R810 Dual Color Multichannel Fiber Photometry with a behavior tracking system (RWD life science).Density functional theory (DFT) calculations done with the Vienna Ab-Initio Package. Solvation energies are calculated using the VASPsol implicit solvation model.
Data analysis	Fiji implementation of ImageJ (Version 1.51) and custom MATLAB (R2020b) were used for in vitro calcium imaging analysis. The custom MATLAB (R2020b) was used for forced swimming tests analysis. R810 Dual Color Multichannel Fiber Photometry with a behavior tracking system (RWD life science) was used for mouse/rat conditioned place preference tests analysis. The custom MATLAB code used in this study is available at https://github.com/kevintang725/Ultrasound-programmable-hydrogen-bonded-organic-frameworks-for-sono-chemogenetics. GraphPad Prism 9.3.1 and Biorender were used as described in the methods section.

For manuscripts utilizing custom algorithms or software that are central to the research but not yet described in published literature, software must be made available to editors and reviewers. We strongly encourage code deposition in a community repository (e.g. GitHub). See the Nature Portfolio guidelines for submitting code & software for further information.

Data

Policy information about availability of data

All manuscripts must include a data availability statement. This statement should provide the following information, where applicable:

- Accession codes, unique identifiers, or web links for publicly available datasets
- A description of any restrictions on data availability
- For clinical datasets or third party data, please ensure that the statement adheres to our policy

The code used to analyse data in the current study is available from the GitHub repository for this article (https://github.com/kevintang725/ultrasound-programmable-hydrogen-bonded-organic-frameworks-for-sono-chemogenetics). Crystallographic data for the structures in this article have been deposited at the Cambridge Crystallographic Data Centre under deposition nos. CCDC 2338302 (HOF-TATB). Copies of the data can be obtained free of charge from https://www.ccdc.cam.ac.uk/structures/. All other data supporting the findings of this study are available within the Article and its Supplementary information and Supplementary Data. Source data are provided with this paper.

Research involving human participants, their data, or biological material

Policy information about studies with human participants or human data. See also policy information about sex, gender (identity/presentation), and sexual orientation and race, ethnicity and racism.

Reporting on sex and gender	This study did not involved human research participants.
Reporting on race, ethnicity, or other socially relevant groupings	This study did not involved human research participants.
Population characteristics	This study did not involved human research participants.
Recruitment	This study did not involved human research participants.
Ethics oversight	This study did not involved human research participants.

Note that full information on the approval of the study protocol must also be provided in the manuscript.

Field-specific reporting

Please select the one below that is the best fit for your research. If you are not sure, read the appropriate sections before making your selection.

☒ Life sciences ☐ Behavioural & social sciences ☐ Ecological, evolutionary & environmental sciences

For a reference copy of the document with all sections, see nature.com/documents/nr-reporting-summary-flat.pdf

Life sciences study design

All studies must disclose on these points even when the disclosure is negative.

Sample size	Sample sizes were determined based on previous studies and are similar to studies published in the filed {DOI: 10.3791/3638; DOI: 10.1038/nature07926; DOI: 10.1038/s41551-022-00862-w; DOI: 10.1038/s41565-019-0521-z}. For in vitro calcium imaging, at least 3 videos were inspect > 100 neurons per experimental condition; for the immunohistological experiments, > 3 mice/rat were treated at different experimental conditions and their tissues were collected for imaging; for fiber photometry tests, at least 3 mice/rat were used per experimental condition; for the forced swimming tests, at least 9 mice were treated per experimental condition; for the conditioned place preference tests, > 5 mice/rat were treated per experimental condition. Sample sizes were selected to achieve at least 80% power at a significance level of 0.05. The details of sample size in each experiment were given in the replication section of methods.
Data exclusions	For the in vitro calcium imaging, the neurons without the designed receptor hM3D(Gq)-mCherry were excluded. for the animal behavior tests, animals with failed surgeries were discarded from further experiments; for the conditioned place preference tests, mice/rats were chosen for tests only if the baseline preference for either side chamber is between 10%-70%, or for the medium chamber is <40%.
Replication	Each in vitro experiment was repeated at least three times per experimental condition. For the in vivo experiment, we utilized at least three subjects per experimental condition. The exact number of replicates for each experiment is detailed in the manuscript and figure captions.
Randomization	Cells were randomly chosen in each experimental condition. Animals were randomized into different experimental groups.
Blinding	The investigators were not blinded during the in vitro and in vivo data collection. Blinding was not necessary in our study since we made no prior assumption on the response of the different samples to the experimental treatment. Samples were all treated in parallel and all samples treated were always measured.

Reporting for specific materials, systems and methods

We require information from authors about some types of materials, experimental systems and methods used in many studies. Here, indicate whether each material, system or method listed is relevant to your study. If you are not sure if a list item applies to your research, read the appropriate section before selecting a response.

Materials & experimental systems

n/a	Involved in the study
☐	☒ Antibodies
☐	☒ Eukaryotic cell lines
☒	☐ Palaeontology and archaeology
☐	☒ Animals and other organisms
☒	☐ Clinical data
☒	☐ Dual use research of concern
☒	☐ Plants

Methods

n/a	Involved in the study
☒	☐ ChIP-seq
☒	☐ Flow cytometry
☒	☐ MRI-based neuroimaging

Antibodies

Antibodies used

Primary antibodies: Rabbit anti-Iba1 (1:500, 013-27691, Wako Chemicals); Rabbit anti-Cleaved Caspase-3 (1:500, 9661, Cell Signaling Tec.); Rabbit anti-GFAP (1:500, 13-0300, Invitrogen); Mouse anti-tyrosine hydroxylase antibody (MA1-24654, Fisher Scientific, 1:1000); Rabbit anti-c-Fos antibody for mice (1:500, ab222699, Abcam); Rabbit anti-c-Fos antibody for rats (1:500, ab289723,Abcam);
Secondary antibodies: Donkey anti-Rabbit, Alexa Fluor 594 (1:500, A32754, Invitrogen); Donkey anti-Rabbit, Alexa Fluor 594 (1:500, A32754, Invitrogen); Donkey anti-Rabbit, Alexa Fluor 594 (1:500, A32754, Invitrogen); Goat anti-mouse Alexa Fluor 488 (1:1000, ab150113, Abcam); Goat anti-rabbit Alexa Fluor 405 (1:500, ab175652, Abcam); Goat anti-rabbit Alexa Fluor 405 (1:500, ab175652, Abcam); H&E staining kit (ab245880, Abcam); Hoechst 33342 (1:5000, 17535, AAT Bioquest)

Validation

The antibodies were validated in previous work and in our laboratory for immunohistological staining on mouse/rat brain slices (mouse : adult, C57BL/6; rat: adult, Long-Evans).

Eukaryotic cell lines

Policy information about cell lines and Sex and Gender in Research

Cell line source(s)

The HEK 293T cell line was generously provided by Dr. Rongze Lu (UT Austin), who originally obtained it from ATCC. Mouse primary cortical neurons were isolated from C57BL/6 mouse embryos.

Authentication

microscopic inspection

Mycoplasma contamination

None of the cell lines were tested for mycoplasma contamination

Commonly misidentified lines
(See ICLAC register)

No commonly misidentified cell lines were used

Animals and other research organisms

Policy information about studies involving animals; ARRIVE guidelines recommended for reporting animal research, and Sex and Gender in Research

Laboratory animals

C57BL/6 mice (20-26 g; 12-16 weeks old; Jackson laboratory) were used in forced swimming tests, C57BL/6 mice (20-26 g; 12-16 weeks old; Jackson laboratory) were used in other our research. 3-4 months old Long-Evans Rats (Charles River) were used in our experiments. Mice and rat used in behavioral experiments were housed in a reversed 12 h light-dark cycle in room set to 21 to 24 ? and 50% humidity.

Wild animals

this study did not include wild animals

Reporting on sex

Female and male mice were included in all experiments irrespective of sex. Female rats were used in this study.

Field-collected samples

this study did not involve samples collected from the field

Ethics oversight

All procedures designed according to the National Institute of Health Guide for the Care and Use of Laboratory Animals, approved by the Institutional Animal Care and Use Committee at the University of Texas at Austin (AUP-2021-00086, AUP-2021-00162 and AUP-2024-00150), and were supported via the Animal Resources Center at the University of Texas at Austin. All the surgery tools were sterilized before the experiments.

Note that full information on the approval of the study protocol must also be provided in the manuscript.

Plants

Seed stocks	No plants were used
Novel plant genotypes	No plants were used
Authentication	No plants were used